Visibility-aware Cooperative Aerial Tracking with Decentralized LiDAR-based Swarms

Longji Yin¹, Yunfan Ren¹, Fangcheng Zhu¹, Liuyu Shi¹, Fanze Kong¹, Benxu Tang¹, Wenyi Liu¹, Ximin Lyu², and Fu Zhang¹

Abstract-Autonomous aerial tracking with drones offers vast potential for surveillance, cinematography, and industrial inspection applications. While single-drone tracking systems have been extensively studied, swarm-based target tracking remains underexplored, despite its unique advantages of distributed perception, fault-tolerant redundancy, and multidirectional target coverage. To bridge this gap, we propose a novel decentralized LiDAR-based swarm tracking framework that enables visibilityaware, cooperative target tracking in complex environments, while fully harnessing the unique capabilities of swarm systems. To address visibility, we introduce a novel Spherical Signed Distance Field (SSDF)-based metric for 3-D environmental occlusion representation, coupled with an efficient algorithm that enables real-time onboard SSDF updating. A general Field-of-View (FOV) alignment cost supporting heterogeneous LiDAR configurations is proposed for consistent target observation. Swarm coordination is enhanced through cooperative costs that enforce inter-robot safe clearance, prevent mutual occlusions, and notably facilitate 3-D multidirectional target encirclement via a novel electrostatic-potential-inspired distribution metric. These innovations are integrated into a hierarchical planner, combining a kinodynamic front-end searcher with a spatiotemporal SE(3)back-end optimizer to generate collision-free, visibility-optimized trajectories. The proposed approach undergoes thorough evaluation through comprehensive benchmark comparisons and ablation studies. Deployed on heterogeneous LiDAR swarms, our fully decentralized implementation features collaborative perception, distributed planning, and dynamic swarm reconfigurability. Validated through rigorous real-world experiments in cluttered outdoor environments, the proposed system demonstrates robust cooperative tracking of agile targets (drones, humans) while achieving superior visibility maintenance. This work establishes a systematic solution for swarm-based target tracking, and its source code will be released to benefit the community.

Index Terms—Aerial swarms, multi-UAV tracking, motion planning, decentralized trajectory optimization.

I. INTRODUCTION

utonomous aerial tracking with UAVs, empowered by advances in onboard sensors and computing, is now extensively applied in fields ranging from cinematography to surveillance and industrial inspection. Recent studies highlight the unique suitability of UAVs for tracking dynamic targets in complex environments, owing to their highly agile three-dimensional (3-D) maneuverability. While substantial progress has been made in single-UAV tracking, the swarm-based aerial tracking remains underexplored. Nevertheless, cooperative UAV swarms surpass the capabilities of individual trackers



Fig. 1. A swarm of four autonomous drones is cooperatively tracking a human runner using heterogeneous LiDAR configurations. The LiDAR setup consists of one upward-facing Mid360 LiDAR (marked by blue dashed lines), one downward-facing Mid360 LiDAR (green dashed lines), and two Avia LiDARs (red dashed lines). The swarm forms a 3-D distribution to track the target, with each tracker positioned optimally to suit its FOV settings.

by exploiting distributed perception, fault-tolerant redundancy, and multidirectional target coverage—features unattainable in single-UAV paradigms. In this work, we bridge this gap by introducing a new framework for visibility-aware target tracking, utilizing a cooperative team of decentralized UAVs.

Effective agile aerial tracking with autonomous swarms primarily relies on three criteria: visibility, coordination, and portability. Visibility, as a fundamental requirement, demands persistent sensor-based observation of the target by the trackers during the flight. Swarm coordination requires the drone to track the target cooperatively without impeding teammate performance. Portability necessitates a scalable and computationally efficient planner to enable real-time deployment on decentralized swarms. In the existing studies, a framework that can effectively fulfill all three criteria is still lacking. As outlined below, three key technical challenges in current swarm tracking systems still limit the tracking performance.

The first challenge lies in designing accurate metrics to quantify the visibility conditions in target tracking tasks. Line-of-sight (LOS) visibility, commonly adopted since it matches with the sensor measurement principles (e.g. LiDAR and camera), imposes two key requisites in aerial tracking: (1) an obstacle-free LOS between tracker and target to prevent occlusions, and (2) LOS alignment within the tracker's field-of-view (FOV) to sense the target. The first requisite needs a robust metric formulation to penalize occlusion and steer the LOS away from obstructed areas, but existing solutions

¹The authors are with the Department of Mechanical Engineering, The University of Hong Kong, Hong Kong. ²X. Lyu is with the School of Intelligent System Engineering, Sun Yat-sen University, Shenzhen, China. Corresponding author: Fu Zhang, fuzhang@hku.hk.

are constrained by many deficiencies like non-differentiable formulations [1], [2], inflexible dependencies on specific FOV shapes [3], [4], and oversimplified 2-D occlusion models [5]. For the second FOV requisite, many studies enforce fixed tracker-target altitude alignment [6]–[8], a heuristic that disregards the FOV geometries and wastes the tracker's vertical agility. Current swarm tracking works rarely consider the FOV configurations in a swarm, ignoring the FOV configurations' critical impact on proper swarm spatial distribution for collective target perception. Thus, developing reliable and effective visibility metrics remains a crucial challenge.

The second challenge is creating metrics to coordinate the swarm tracking maneuvers in 3-D space. Beyond ensuring inter-agent safety, effective coordination in swarm tracking entails two more objectives: mutual occlusion avoidance and multi-angle target coverage. Each drone must prevent blocking teammates' LOS to the target, ensuring persistent collective visibility during tracking. Concurrently, the swarm needs to optimize spatial distribution to enable multidirectional target coverage, which mitigates single-direction occlusions, supports target measurement fusion from diverse perspectives, and grants each tracker a larger angular space to respond to adverse situations. This multidirectional approach can also maximize the utility of heterogeneous sensors by positioning agents at vantage points suited to their FOV modalities. The existing frameworks, however, either disregard these cooperation issues or rely on simplistic 2-D equidistant leader-follower formations to separate the trackers. Such strategies waste the swarm's 3-D maneuverability, constraining agents to planar configurations that limit the volumetric coordination potential.

The third technical challenge involves the decentralization of the whole swarm tracking system. Decentralized architecture underpins the scalability, fault tolerance, and efficient use of computational resources. However, unlike centralized approaches, where a single entity directly manages the entire swarm, decentralization introduces more challenges in coordinating swarm behavior. A decentralized swarm demands adaptive individual planners that reconcile local motion with global swarm objectives, coupled with solid system architectures supporting peer-to-peer communication and scalable computation. Meanwhile, collaborative perception, where agents exchange sensory data to collectively enhance tracking robustness, is also vital to the performance of a decentralized system.

Based on the above analysis and insights, we propose a complete swarm tracking system that addresses all the outlined challenges. To resolve the LOS occlusion challenge, we novelly adapt the Spherical Signed Distance Field (SSDF), a spatial representation originally used for graphical rendering [9]–[12], into a visibility metric that encodes the 3-D environmental occlusion around the target. The metric's practicality is supported by our efficient SSDF update algorithm tailored for real-time tracking operations. A differentiable SSDF-based occlusion penalty is derived for visibility-aware trajectory optimization. To ensure FOV alignments, we formulate a unified FOV constraint supporting heterogeneous LiDAR configurations. To tackle the mutual occlusion challenge, we regulate a minimum angular separation clearance between the swarm members around the target. For uniform 3-D multidirectional

target encirclement, we draw inspiration from Thomson's classical electron distribution problem, innovatively framing the optimal swarm distribution as minimizing the electrostatic potential energy of charged particles (UAVs) repelling each other around a central nucleus (the target). Unlike plain 2-D equidistant formations in existing works [6]–[8], [13]–[15], our formulation achieves true 3-D distribution enclosing the target. Additional metrics quantifying the tracking distance, obstacle avoidance, dynamic feasibility, and inter-agent collision avoidance are also formulated to assess the tracking motion.

We incorporate our proposed metrics into a two-stage decentralized planning framework consisting of a front-end kinodynamic path searcher and a back-end spatiotemporal trajectory optimizer. Given a sequence of target future positions interpolated by the prediction module, the kinodynamic searcher generates discrete candidate paths by expanding motion primitives temporally aligned with the target's prediction stamps. The searcher determines the optimal guiding path by assessing the primitives against the proposed tracking metrics. In the back-end stage, a corridor-constrained spatiotemporal optimizer generates an executable tracking trajectory along the front-end path. Since the tracker's 3-D FOV is governed by both its position and orientation, we perform SE(3) full-state optimization for the back-end. By embedding our metrics in both stages, the planning framework systematically trades off safety, visibility, and spatial coordination, enabling cooperative visibility-aware swarm tracking in dense environments.

At the system level, we present a fully decentralized swarm architecture, incorporating decentralized localization, mapping, planning, and control modules to address the third outlined technical challenge of decentralization. Trajectories are synchronized over a wireless network to facilitate tight swarm coordination. Real-time local mapping data and target measurements from individual drones are shared among the swarm to enable distributed collaborative perception. We rigorously validate the proposed planner through comprehensive simulation tests. Comparative benchmark against cutting-edge methods confirms our planner's superior ability to maintain persistent target visibility. Integrating the modules into decentralized swarms with heterogeneous LiDAR FOVs, we conduct extensive real-world experiments in different complex environments, successfully achieving cooperative tracking of agile targets (drones, human runners). Notably, the swarm demonstrates dynamic reconfigurability (agent joining/leaving) during live target tracking in constrained outdoor scenarios, highlighting advanced decentralization and system robustness.

The contributions of this paper are listed as:

- A novel Spherical Signed Distance Field (SSDF)-based environmental occlusion representation is proposed for target tracking, coupled with an efficient SSDF update algorithm that enables real-time onboard computation.
- New differentiable metrics for line-of-sight (LOS) visibility assessment are developed, including an SSDFderived occlusion penalty and a general FOV alignment cost adaptable to heterogeneous FOV settings.
- Novel differentiable swarm coordination metrics are formulated for cooperative tracking, notably an electrostatic

potential-inspired swarm distribution cost enabling true 3-D multidirectional target encirclement.

- 4) A two-stage planning framework is designed, comprising a kinodynamic front-end searcher and a spatiotemporal SE(3) back-end optimizer, systematically trading off the metrics for visibility-aware cooperative swarm tracking.
- 5) A complete decentralized multi-UAV tracking system is presented, featuring collaborative perception, decentralized planning, and dynamic swarm reconfiguration. Rigorous simulations and real-world experiments demonstrate its robust performance in complex environments.
- The source code of the proposed system will be publicly released for the reference of the research community.

In what follows, we review related works in Sec.II and provide a system overview in Sec.III. The SSDF-based spatial visibility representation and update algorithms are introduced in Sec.IV. Planning metrics for visibility-aware swarm tracking are formulated in Sec. V, followed by details on front-end kinodynamic searching and back-end trajectory optimization in Secs. VI and VII. Benchmark and experimental results are given in Sec.VIII and Sec.IX. Sec.X concludes this work.

II. RELATED WORKS

A. Single-UAV Target Tracking

Several earlier studies [16], [17] treat vision-based aerial tracking as a local control problem, designing control laws to regulate feedback error in image spaces. However, these control laws struggle to account for constraints like visibility and cannot plan for future target motions over a horizon. Han et al. [18] proposed an optimized-based tracking planner consisting of a spatiotemporal optimizer and kinodynamic searcher, but they only focus on maintaining tracking distance while neglecting visibility. Penin et al. [19] formulate a nonlinear MPC problem which penalizes the occlusion using the obstacle projection on the image plane. However, their method assumes ellipsoid-shaped obstacles, limiting the application to unstructured scenes. Bonatti et al. [20] developed an aerial cinematography framework considering obstacle avoidance, LOS visibility, and smoothness, but ignored the sensor's FOV geometry in visibility constraints. In [3], Wang et al. design an occlusion cost that penalizes the intersection area of obstacles and the FOV, aiming to eliminate all such intersections. However, the proposed constraint is too strict to be satisfied in dense spaces. Besides, their cost is specifically formulated for conic FOVs and not compatible with omnidirectional sensors like 360° LiDARs, as the obstacle-intersection area can always exist in the omnidirectional view. Jeon et al. [2] present a visibility metric based on ESDFs. They assess the risk of occlusion by evaluating the minimum ESDF value along the tracker-target LOS. However, their visibility metric lacks differentiability, making it unsuitable for back-end optimization. Ji et al. [5] propose a new method, which generates a sequence of 2-D sector-shaped visible regions for visibilityaware tracking. But these 2-D sectors represent visibility only at a specific height, which is unable to facilitate 3-D occlusion avoidance. Additionally, the seed (tracker position) for building visibility sectors must be in visible areas, making it impossible to quantify visibility when the seed is already occluded. This is unfavorable for target-shared swarm tracking, as trackers can temporarily endure occlusion but still require an instructive effort within the occluded area to escape it. To systematically tackle all the above drawbacks, we novelly adopt Spherical Signed Distance Fields (SSDFs) [9]–[11], [21] to encode the 3-D spatial visibility around the tracked target. Our metric formulation is differentiable, remains independent of any specific FOV type, and models full 3-D visibility without seed restrictions. Moreover, a general geometric constraint for target-FOV alignment is designed to prevent visibility loss caused by heterogeneous FOV shapes.

B. Multiple-UAV Target Tracking

Motion planning for multi-UAV target tracking has gained growing interest in recent research [6], [8], [13], [22]-[25]. Zhou et al. [6] present a swarm of drones tracking a target using a fixed 2-D leader-follower formation, where the target's position, observed by one tracker, is shared with others to enhance occlusion resistance. In [13], Tallamraju et al. employ a 2-D equidistant formation to minimize fused uncertainty in target estimation and use model predictive controllers (MPC) for both formation control and obstacle avoidance. While the drones in [6], [13] share target observations to temporarily endure occlusion, they lack strategies to proactively mitigate visibility loss. To address this, Nageli et al. [24] propose an MPC-based framework that uses a horizon plane, derived from obstacles, to separate visible and invisible regions. However, their approach assumes obstacles are ellipsoidal, making it unsuitable for arbitrarily shaped obstacles. In [8], Lee et al. check the occupancy along the LOS to avoid obstacle occlusion and employ 2-D Inter-Visibility Cells (IVC) to prevent the inter-agent occlusion. However, they only consider the target visibility at the front-end stage but conduct pure path smoothing in the back-end. Such inconsistency could still lead to constraint violation on final trajectories. Bucker et al. [22] divide the space around the target into discrete cells, assigning each cell a score based on its occlusion avoidance potential. A centralized greedy algorithm is then used to generate motion sequences that minimize visibility loss for each drone. However, the predefined priority in their greedy search can result in sub-optimal outcomes. Ho et al. [23] propose a framework for generating swarm trajectories in aerial 3-D reconstruction. Their approach allows the follower formation to rotate around the target, with a centralized front-end planner using dynamic programming to find the optimal sequence of the rotation angles. Nonetheless, the fixed formation assumption is prone to failure in cluttered environments, and the centralized design is susceptible to node failures. The existing multi-UAV tracking works [6]-[8], [14], [15], commonly suggest a 2-D equidistant swarm formation to encircle the target. However, such 2-D formations severely waste the 3-D maneuverability of UAVs and may oppose other tracking requirements like the FOV constraint. To address this deficiency, we draw inspiration from a classic electrostatic problem and design a novel metric to instruct the uniform 3-D swarm encirclement in real 3-D spaces. Unlike

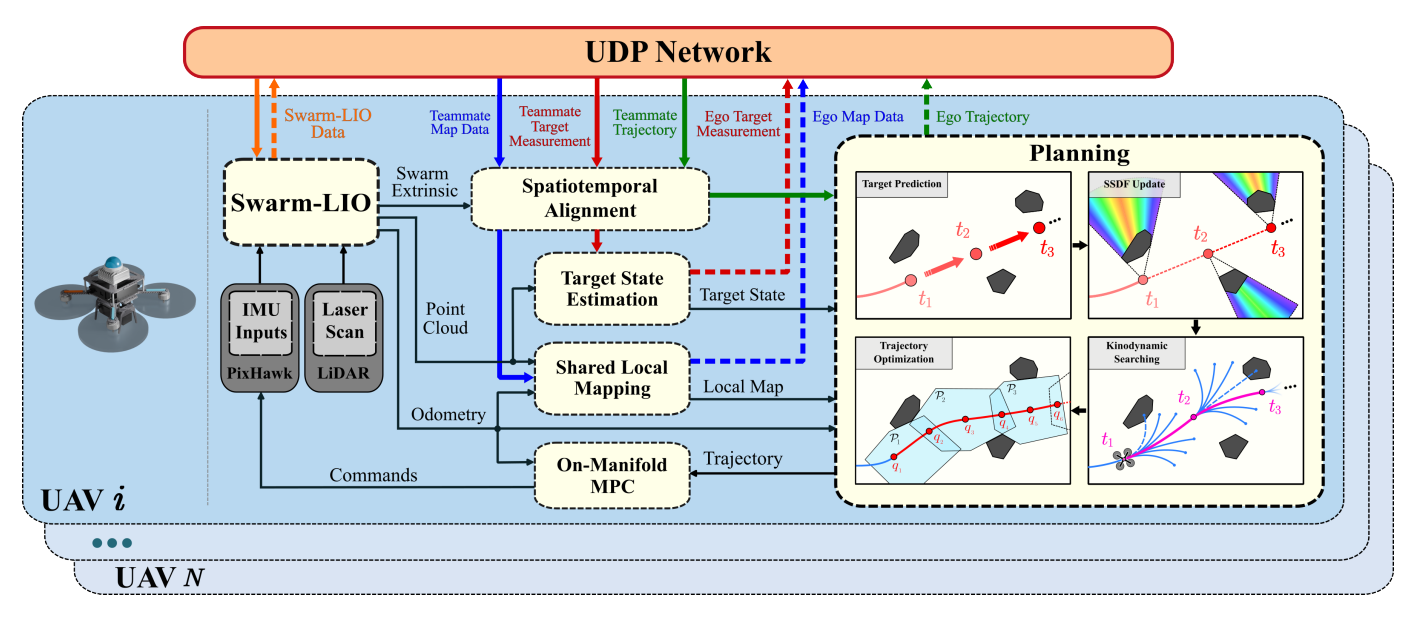


Fig. 2. An overview of our complete decentralized swarm tracking system, including the decentralized swarm localization, shared mapping, collaborative target estimation, onboard control, and motion planning modules. A hierarchical planner is designed to generate optimal trajectories for swarm tracking. All critical operational data is exchanged between swarm members via a UDP-based wireless network.

the centralized approaches [22], [23], our method adopts a fully decentralized framework, where the formation is encoded as a slack cost to enable a flexible trade-off between swarm distribution and other objectives. Despite being decentralized, our approach ensures cooperative maneuvers among the drones while consistently preserving high visibility of the target.

III. SYSTEM OVERVIEW

The overall autonomous swarm tracking system is illustrated in Fig.2. This decentralized swarm system aims to cooperatively track a passive target in unknown, cluttered environments using onboard LiDAR sensors. Each drone employs Swarm-LIO [26], a decentralized swarm LiDARinertial odometry, for self-localization and mutual state estimation. The drones in the swarm exchange critical operational data with their teammates via a wireless UDP network and transform the received data into the local frame through spatiotemporal alignment, using swarm extrinsics and calibrated system time lag from Swarm-LIO. Besides the data used by Swarm-LIO, three types of information are shared: planned trajectories, local map data, and target measurements. Trajectories are broadcast for swarm cooperation. Each drone receives its teammates' trajectories to formulate the coordination constraints and optimizes its own motion plan accordingly. For local mapping, the system uses an occupancy grid map [27] as the map format. The local map updates of each agent are synchronized across the swarm using a bandwidth-efficient method [28], allowing the trackers to enhance environmental perception collectively. In this work, the target is identified by high-reflective markers, with its position measured by clustering the sensed point clouds. Each tracker shares its target measurements with teammates, while a Kalman filter on each drone fuses its own measurements with those received from others, enabling multi-source robust target state estimation. More system details are presented in Sec.IX-A.

The planning of local tracking trajectories is hierarchical. Given the fused target states, the prediction module first generates a sequence of target future positions via velocity-based linear interpolation with fixed time intervals. An SSDF is then built at each predicted target position to model 3-D occlusion and enable visibility-aware planning (Sec.IV). Collectively considering all the tracking metrics proposed in Sec.V, we employ a kinodynamic searcher to expand motion primitives and select an optimal path (Sec.VI), used for safe corridor generation and back-end trajectory initialization. Afterwards, the trajectory's spatial and temporal profiles are efficiently optimized by the back-end to maximize the tracking performance (Sec.VII). The planning process cycles periodically with a receding horizon, and the generated trajectories are finally executed via a model predictive controller [29].

IV. SPHERICAL SIGNED DISTANCE FIELD

We introduce a novel visibility-aware approach for target tracking that utilizes the Spherical Signed Distance Fields (SSDFs). Traditionally applied as a visibility model for spatial shading in computer graphics [9]–[11], SSDFs inherently align with visibility problems through their radial environmental representation centered at the focal point (the target). Lines of sight emanating from the target partition the space into visible and occluded sectors. At a specified tracking distance (radius), the degree of occlusion can be indicated by the signed spherical distance from the tracker's position to the closest visible sector boundaries. This section details our efficient SSDF updating method for real-time visibility-aware planning.

A. Visibility Map Update

To construct an SSDF around the target, we first need to spherically parameterize the 3-D space and update a visibility map around the target. The visibility map, denoted as \mathcal{V} , is a 3-D grid where each cell has a binary state: a state of 1 means

it is visible, while 0 signifies its occlusion from the target. The visibility map is discretized into a spherical grid defined by θ (polar/latitudinal angle), ϕ (azimuthal/longitudinal angle), and r (radial distance), with the target position as the grid's origin. Here, θ_i , ϕ_j , and r_k represent the respective indices of these parameters. Fig.3(a) shows the spherical grid. LOS visibility has a clear yet useful property: for a given direction (θ, ϕ) , visibility deteriorates monotonically as the radial distance rincreases. If the LOS along the direction (θ, ϕ) is firstly blocked by an obstacle located at $[\theta, \phi, r_{min}]_S$, then all positions $[\theta, \phi, r]_S$ with $r > r_{min}$ are also occluded. Fig.3(b) shows this property. We use $[\cdot]_S$ to denote the spherical coordinates. Observing this monotonic property, we can update the visibility map by identifying the closest occluded radius r_{min} for each direction (θ_i, ϕ_i) , denoting the radial index of r_{min} as k_{min} . In Alg.1, we traverse the occupancy map \mathcal{C} around the target within a radius r_{max} and select the smallest k_{min} for every direction by comparison. Then, along each direction in map \mathcal{V} , the grids with radial index k greater than the minimal occluded index k_{min} can be directly set as occluded by **setOcclusion()**. The auxiliary array S in Line 13 is prepared for the further updates in Sec.IV-C.

Algorithm 1 Visibility Map Update

Notation: the grid map \mathcal{C} and cells \mathbf{c} in \mathcal{C} ; the visibility map \mathcal{V} discretized by latitude θ_i , longitude ϕ_j , and radial distance r_k ; the index of closest occluded radial distance $k_{min}[i,j]$ for direction (θ_i,ϕ_j) ; The resolution N_r of the radial dimension r; An auxiliary array S of length N_r ;

Ensure: the visibility map V is updated;

```
1: Initialize: k_{min} \leftarrow (N_r - 1),
2: for each c in C do
3:
         if cell c is occupied then
               [\theta_i, \phi_j, r_k]_S \leftarrow \text{ToSphericalCoordinate}(\mathbf{c});
4:
               if k_{min}[i,j] > k then
 5:
                    k_{min}[i,j] \leftarrow k;
 6:
               end if
 7:
         end if
8:
 9: end for
10: for each direction (\theta_i, \phi_i) in \mathcal{V} do
11:
         h \leftarrow k_{min}[i,j];
         setOcclusion(\mathcal{V}, h);
12:
          S[h].PUSH((\theta_i, \phi_i));
14: end for
```

B. 2-D Spherical Distance Transform

In this section, we introduce how to update a 2-D SSDF from a 2-D visibility map parameterized by θ and ϕ . A 2-D visibility map layer \mathcal{V}_r can be extracted from the 3-D map \mathcal{V} by fixing the radial dimension to a specific r. Then the obtained 2-D layer \mathcal{V}_r describes the visibility of all directions at radius r.

Given two directions $\mathbf{v}(\theta, \phi)$ and $\mathbf{u}(\theta', \phi')$ on \mathcal{V}_r , the angular distance \mathcal{L} between these two directions is given by the spherical law of cosine:

$$\mathcal{L}\{\mathbf{v}, \mathbf{u}\} = \cos^{-1}(\cos \theta' \cos \theta + \sin \theta' \sin \theta \cos |\phi - \phi'|). \quad (1)$$

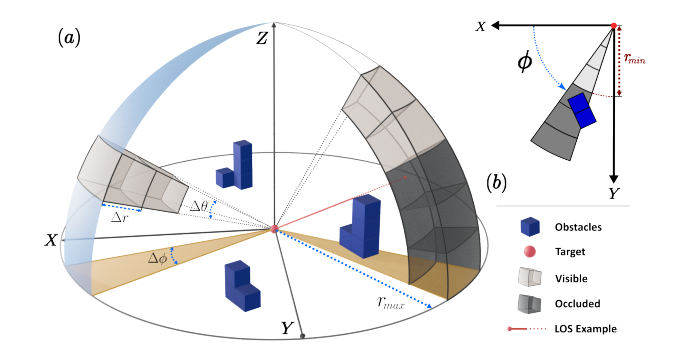


Fig. 3. (a) An illustration of the spherical discretization and the definition of the visibility map. A map cell is flagged as occluded if obstacles block the LOS. (b) An illustration of the monotonic property used in visibility maps. Along the direction $(0,\phi)$ in the figure, an obstacle blockage is at radius r_{min} . Then all grids with radii larger than r_{min} can be directly set as occluded.

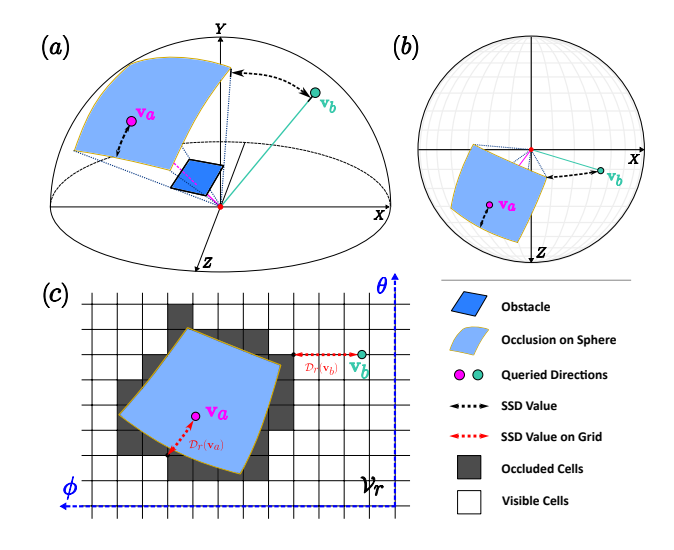


Fig. 4. Illustrations of the SSDF definition. (a) On the surface of a unit sphere, an occluded area is shadowed by an obstacle. For two queried directions \mathbf{v}_a and \mathbf{v}_b , the black dashed curves on the sphere indicate the directions' Spherical Signed Distances (SSD) to the closest visibility boundary. (b) A top-down view of figure (a). (c) The corresponding occluded cells on the discretized 2-D θ - ϕ grid. The red dashed curves indicate the SSDF values of the queried directions \mathbf{v}_a and \mathbf{v}_b on the discrete grid.

A 2-D spherical distance field \mathcal{D}_r is a more informative visibility model based on \mathcal{V}_r , where for a queried direction \mathbf{v} , it stores a signed angular distance to the direction's closest visibility boundary. According to [9]–[11], it is defined as

$$\mathcal{D}_{r}(\mathbf{v}) = \begin{cases} + \min_{\mathcal{V}_{r}(\mathbf{u}) = 0} \mathcal{L}\{\mathbf{u}, \mathbf{v}\}, & \mathcal{V}_{r}(\mathbf{v}) = 1, \\ - \min_{\mathcal{V}_{r}(\mathbf{u}) = 1} \mathcal{L}\{\mathbf{u}, \mathbf{v}\}, & \mathcal{V}_{r}(\mathbf{v}) = 0, \end{cases}$$
(2)

where \mathbf{u} is a direction vector. By definition, SSDFs can quantify the degree of occlusion using the distance value, enabling trackers to query the minimum angular distance required to escape occluded regions. Fig.4(a)-(b) illustrate the definition, and Fig.4(c) shows the 2-D θ - ϕ grid for discrete distance transform. Euclidean Signed Distance Fields (ESDFs) are widely used in navigation. The update algorithms of ESDFs are based on dimensionality reduction [30]–[33]. However, unlike 2D ESDFs, the non-Euclidean and asymmetric nature of the 2D θ - ϕ spherical grid in SSDFs prevents direct application

of these algorithms. Nevertheless, as shown in [11], SSDFs can still be correctly updated by reducing dimensions in a specific order: first scanning latitudes, then longitudes.

We provide an overview of the algorithm in [11] for clarity, which is a spherical version of [30] following a certain scanning order. By definition in Eq.2, updating the spherical distance transform needs to find the closest visibility boundary for all the discretized directions $\mathbf{v}(\theta_i,\phi_j)$. The process takes two phases. The first phase is scanning every latitudinal column θ_i . Along each latitude θ_i , we traverse all the longitudes (θ_i,ϕ_j) to find each ϕ_j 's closest longitudinal visibility boundary ϕ_j^{cls} that minimizes the objective $\mathcal{L}\{(\theta_i,\phi_j),(\theta_i,\phi_j^{cls})\}$. This is a 1-D distance transform, which can be updated by Alg.2, a variant of the L_1 -distance transform algorithm in [30]. In Alg.2, the array g[i,j] records the updated closest visible boundary direction (θ_i,ϕ_j^{cls}) for each ϕ_j along latitude θ_i . Initially, all entries in array g are assigned a virtual direction NULL, where the distance from any direction to NULL is defined as infinite.

Algorithm 2 Latitudinal Scan

Notation: the visibility map \mathcal{V}_r discretized by by latitude θ_i and longitude ϕ_j ; The latitudinal resolution N_{θ} and the longitudinal resolution N_{ϕ} ; An auxiliary direction h;

Ensure: the array g is correctly updated;

```
1: Initialize: g \leftarrow NULL,
 2: for i=0 to N_{\theta}-1 do
          for j=0 to N_{\phi}-1 do
               if V_r(\theta_i, \phi_j) is visible then
 4:
                    g[i,j] \leftarrow (\theta_i,\phi_j);
 5:
 6:
                    g[i,j] \leftarrow g[i,j-1];
 7:
 8:
          end for
 9:
          h \leftarrow g[i, N_{\phi} - 1];
10:
          for j = N_{\phi} - 1 to 0 do
11:
               if \mathcal{L}\{g[i,j],(\theta_i,\phi_j)\} < \mathcal{L}\{h,(\theta_i,\phi_j)\} then
12:
                     h \leftarrow g[i,j];
13:
               end if
14:
15:
               g[i,j] \leftarrow h;
16:
          end for
17: end for
```

After deriving ϕ_j^{cls} in the first phase, the second phase updates the other dimension, θ_i , to minimize the angular distance objective in Eq.1. To achieve the second phase, we conduct a variant of the L_2 -distance transform scanning in [30] along each longitude ϕ_j , as detailed in Alg.3. While the distance objective $\mathcal L$ is not strictly an L_2 -distance, it shares the same single intersection property [11], enabling the variant L_2 -distance algorithm from [30] to be applied. For two distinct directions $\mathbf v_1(\theta_1,\phi_1)$ and $\mathbf v_2(\theta_2,\phi_2)$, and a given longitude ϕ_0 , the function $\Theta(\mathbf v_1,\mathbf v_2,\phi_0)$ in Alg.3 computes a latitude θ_0 . At this latitude, the direction $\mathbf v_0(\theta_0,\phi_0)$ satisfies $\mathcal L\{\mathbf v_1,\mathbf v_0\}=\mathcal L\{\mathbf v_2,\mathbf v_0\}$. The single intersection property ensures that $\mathbf v_0$ is the only intersection where the distances

Algorithm 3 Longitudinal Scan

Notation: the visibility map V_r discretized by latitude θ_i and longitude ϕ_j ; The latitudinal resolution N_{θ} and the longitudinal resolution N_{ϕ} ; Two auxiliary arrays v and z; The array B[i,j] recording closest visibility boundaries.

Ensure: the closest boundary D is correctly updated;

```
1: for j = 0 to N_{\phi} - 1 do
         n \leftarrow 0;
         v[0] \leftarrow 0;
 3:
         z[0] \leftarrow -\infty;
 4:
 5:
         z[1] \leftarrow +\infty;
         for i=1 to N_{\theta}-1 do
 7:
               h \leftarrow \Theta(g[i,j],g[v[n],j],j);
               while h \leq z[n] do
 8:
 9:
                   n \leftarrow n-1;
                    h \leftarrow \Theta(g[i,j],g[v[n],j],j);
10:
               end while
11:
               n \leftarrow n + 1;
12:
               v[n] \leftarrow i;
13:
14:
               z[n] \leftarrow h;
               z[n+1] \leftarrow +\infty;
15:
16:
         end for
         n \leftarrow 0
17:
         for i=0 to N_{\theta}-1 do
18:
               while z[n+1] < i do
19:
                   n \leftarrow n + 1
20:
               end while
21:
               B[i,j] \leftarrow g[v[n],j];
22:
         end for
23:
         resetAuxiliaryArrays();
24:
25: end for
```

from \mathbf{v}_1 and \mathbf{v}_2 are equal. The latitude θ_0 is given by

$$\Theta(\mathbf{v}_{1}, \mathbf{v}_{2}, \phi_{0}) = \begin{cases} \pi/2, & P = Q, \\ \tan^{-1}(\frac{R}{P-Q}), & \frac{R}{P-Q} \ge 0, \\ \tan^{-1}(\frac{R}{P-Q}) + \pi, & \frac{R}{P-Q} < 0, \end{cases}$$
(3)

where $P = \sin \theta_1 \cos(\phi_1 - \phi_0)$, $Q = \sin \theta_2 \cos(\phi_2 - \phi_0)$, and $R = \cos \theta_2 - \cos \theta_1$. In Alg.3, the array B[i,j] records the final closest visibility boundary for each direction (θ_i,ϕ_j) . Then the spherical distance transform \mathcal{D}_r of direction (θ_i,ϕ_j) is the distance to direction B[i,j]. For more details of this two-phase algorithm, readers can refer to [11] and [30].

During target tracking, trackers should maintain LOS visibility to the target. In visible regions where $\mathcal{V}_r=1$, the LOS visibility constraints are already satisfied. Thus, in practice, we can solely focus on updating the distance fields of invisible areas. The updated spherical distances are then used to penalize the tracker's trajectories within these occluded regions, preventing visibility loss. The necessary angular clearance around the invisible area can be achieved by inflating the occluded grid when updating the visibility map \mathcal{V} . Thus, under this updating rule, the definition in Eq.2 is reformulated as:

$$\mathcal{D}_r(\mathbf{v}) = \begin{cases} 0, & \mathcal{V}_r(\mathbf{v}) = 1, \\ -\min_{\mathcal{V}_r(\mathbf{u}) = 1} \mathcal{L}\{\mathbf{u}, \mathbf{v}\}, & \mathcal{V}_r(\mathbf{v}) = 0. \end{cases}$$
(4)

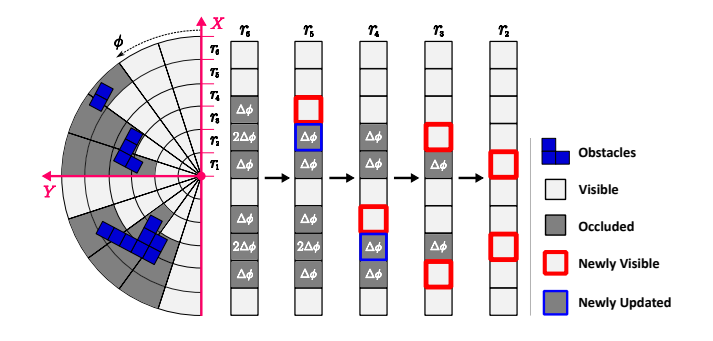


Fig. 5. An illustration of the incremental SSDF update strategy on a 2-D visibility map. The SSDF is updated layer by layer, starting from the outermost 1-D visibility layer at r_0 to the innermost layer at r_1 . Proceeding to each layer, only the newly visible cells (in red boxes) and value-changed cells (in blue boxes) are identified and updated to compute the SSDF. In this example, only two cells in blue boxes require new value calculations throughout the update.

Using this definition, the two-phase algorithm can be applied exclusively to the occluded areas, reducing the computation by skipping updates for visible directions where $\mathcal{V}_r=1$. Although the spherical distance in Eq.4 is truncated, we still refer to the updated distance field \mathcal{D}_r as the "SSDF".

C. Incremental 3-D SSDF Update

In Sec.IV-B, we introduced the two-phase algorithm for updating the SSDF \mathcal{D}_r of a 2-D visibility map \mathcal{V}_r , where \mathcal{V}_r is a single layer extracted from the 3-D visibility map \mathcal{V} by fixing the radial distance r. Our next goal is to update the complete SSDF \mathcal{D} for the entire map \mathcal{V} , enabling the trackers to query the visibility in 3-D space by $\mathcal{D}(\mathbf{p})$. $\mathcal{D}(\mathbf{p})$ is defined by the value of the corresponding 2-D SSDF layer at $r_{\mathbf{p}}$:

$$\mathcal{D}(\mathbf{p}) = \mathcal{D}_{r_{\mathbf{p}}}(\mathbf{v_{\mathbf{p}}}),\tag{5}$$

where $\mathbf{p} \in \mathbb{R}^3$ is the queried position, $r_{\mathbf{p}}$ is the radial distance at position \mathbf{p} , and $\mathbf{v}_{\mathbf{p}}$ is the direction vector at \mathbf{p} . A straightforward approach to update the complete 3-D SSDF \mathcal{D} is traversing all the radial distances r_k discretized in \mathcal{V} and repetitively applying the two-phase algorithm to the 2-D SSDF layer at each r_k . However, this brutal approach leads to large overall computational overhead, especially when the resolution of r_k is high. Thus, there is a necessity for a more efficient method to construct the 3-D SSDFs.

As discussed in Sec.IV-A, LOS visibility has a crucial monotonic property: along each direction (θ_i, ϕ_i) , visibility decreases as the radial distance r_k increases. Thus, among all the 2-D visibility map layers in V, the outermost layer $\mathcal{V}_{r_{max}}$ at radial distance r_{max} has the fewest visible grids. As the radial distance r_k decreases from r_{max} towards the origin, the number of visible grids in layer \mathcal{V}_{r_k} increases monotonically. Drawing inspiration from incremental updates for ESDFs [34]-[37], we propose an incremental strategy for 3-D SSDF computation leveraging this monotonic property. Let N_r denote the resolution of the radial dimension. We begin by updating the 2-D SSDF of the outermost visibility map layer $V_{r_{max}}$ at radial index $k = N_r - 1$ using the twophase algorithm. Then, for the next inner layer at $k = N_r - 2$, which must contain the same or more visible grids, we simply need to insert the newly incremented visible grids from the current layer into the SSDF of the last outermost layer. This incremental insertion process continues sequentially, with each layer being updated based on the SSDF of the previous one, until the innermost layer, with index k=0, is completed. Fig.5 illustrates our incremental strategy using a 2-D visibility map.

To implement our strategy, the incremental algorithm in FI-ESTA [34] is adopted. Given that our strategy solely concerns the insertion operation, we only use the *insertOueue* in [34] to hold the newly incremented visible grids of each layer. These increments have already been collected in Alg.1 within an auxiliary array S of length N_r , where the entry S[k] contains all the directions whose state changes from occluded to visible at the k^{th} layer. In Alg.4, we employ the Breadth-First-Search (BFS) method in [34] to insert these newly visible directions at the k^{th} layer into the SSDF of the previous $(k+1)^{\text{th}}$ layer. Two arrays, B[i,j] and $\mathcal{D}[i,j]$, record the grid (θ_i,ϕ_j) 's closest visibility boundary and its spherical distance transform. BFS is used to update the neighbors by comparison. Since the BFSbased incremental algorithm cannot be perfectly accurate, as analyzed in [34], a comparison with the ground-true SSDF values is provided in Sec.VIII-E to numerically validate the proposed algorithm. By sequentially applying Alg.4 to the layers from the $(N_r-2)^{\text{th}}$ to the innermost one, every grid in the 3-D visibility map V is assigned a spherical distance value, completing the update of the entire 3-D SSDF $\mathcal{D}(\mathbf{p})$. Fig.6 visualized an example of updated SSDF.

Algorithm 4 Incremental SSDF Update

Notation: insertQueue as the queue for SSDF inserting; k is the radial index of the current SSDF layer to update; The array B[i,j] records grid (θ_i,ϕ_j) 's closest visibility boundary; The array $\mathcal{D}[i,j]$ records the spherical distance transform at (θ_i,ϕ_j) ; Arrays B and \mathcal{D} are initialized by the results of the previous $(k+1)^{th}$ layer;

```
Ensure: the SSDF of the k^{th} layer is updated;
```

1: **Initialize:** $insertQueue \leftarrow Empty$;

```
2: for each newly visible direction (\theta_i, \phi_i) in S[k] do
 3:
          B[i,j] \leftarrow (\theta_i,\phi_j);
         \mathcal{D}[i,j] \leftarrow 0;
 4:
 5:
         insertQueue.PUSH((\theta_i, \phi_i));
 6: end for
 7: while insertQueue not empty do
          (\theta_i, \phi_i) \leftarrow insertQueue.FRONT();
 8:
 9:
         insertQueue.POP();
10:
         for each neighbor (\theta_m, \phi_n) of (\theta_i, \phi_i) do
               if \mathcal{L}\{B[i,j],(\theta_m,\phi_n)\}<\mathcal{D}[m,n] then
11:
                    B[m,n] \leftarrow B[i,j];
12:
                    \mathcal{D}[m,n] \leftarrow \mathcal{L}\{B[i,j], (\theta_m,\phi_n)\};
13:
14:
                    insertQueue.PUSH((\theta_m, \phi_n));
15:
               end if
         end for
16:
17: end while
```

D. SSDFs Update on Target Prediction

The last subsections outlined the procedures to update an SSDF around a target in 3-D spaces. To apply these SSDFs

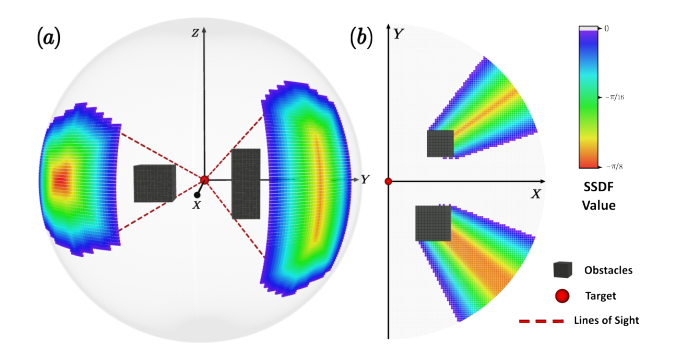


Fig. 6. An example of the SSDF computed for an occluded scene. (a) The SSDF values on the outermost spherical surface. (b) The horizontal cross-section of the updated SSDF at the X-Y plane.

in target tracking, we first predict the target's movements over a future time horizon. A linear velocity-based interpolation module is employed to render a sequence of future target positions according to a time step δT and a prediction horizon T_p . The target position sequence is expressed as

$$Q_{target} = \{ \boldsymbol{\xi}_k \in \mathbb{R}^3 \mid 0 \le k \le N_p, \ t_k = k \cdot \delta T \}, \quad (6)$$

where N_p is the total prediction step number and t_k is the timestamp corresponding to the target position at the k^{th} step from now. To ensure SSDF-based visibility constraints throughout the tracking, we update SSDFs at every predicted position $\boldsymbol{\xi}_k$. As the computations for these N_p SSDFs are independent, they are updated in parallel, keeping the overall computation time efficient. To enable gradient-based optimization with SSDFs, we perform interpolation on the SSDFs to generate the required distance gradients. The application of SSDF for visibility-aware planning is detailed in Sec.V.

V. VISIBILITY-AWARE COOPERATIVE SWARM TRACKING

Incorporating the target's visibility into planning is essential for robust aerial tracking of passive targets. To ensure continuous target observation, trackers must avoid environmental occlusions, maintain an appropriate tracking distance, and keep the target positioned in the sensor's FOV. Meanwhile, the swarm system necessitates the planner to effectively coordinate the multiple trackers, such that each drone can avoid teammate occlusion and make full use of the space surrounding the target. In this section, we introduce several cost functions that model these metrics for swarm tracking. These costs will be utilized in our front-end searching and back-end optimization to quantify the tracking performance. In what follows, the ego drone's position is denoted as $\mathbf{p} \in \mathbb{R}^3$ and assigned as the i^{th} drone in the swarm, with the target position $\boldsymbol{\xi} \in \mathbb{R}^3$. N denotes the number of drones in the swarm, and \mathbf{p}_i denotes the position of the j^{th} drone in the swarm.

A. Environmental Occlusion Cost

This cost \mathcal{J}_{vis} is introduced to preserve the target's LOS visibility against static obstacle occlusions. The occlusion relationships in the environment w.r.t. the target are encoded by

an SSDF introduced in Sec.IV. The environmental occlusion cost at position \mathbf{p} is designed as

$$\mathcal{J}_{vis} = -\mathcal{D}(\mathbf{p}). \tag{7}$$

As stated in Sec.IV, $\mathcal{D}(\mathbf{p})$ returns the angular distance to the closest visibility boundary around \mathbf{p} if it is occluded, otherwise $\mathcal{D}(\mathbf{p})$ returns zero. Both the front-end searching and back-end optimization use this cost to impose penalties on the occluded areas, thereby preventing visibility loss. To conduct numerical optimization with \mathcal{J}_{vis} , we derive the cost gradient as

$$\partial \mathcal{J}_{vis}/\partial \mathbf{p} = -\nabla \mathcal{D}(\mathbf{p}),$$
 (8)

where $\nabla \mathcal{D}(\mathbf{p})$ is the interpolated gradient of SSDF at point \mathbf{p} .

B. Field-of-View Cost

This field-of-view (FOV) cost is to ensure that the LOS between the target and tracker can always remain within the LiDAR's FOV during the flight, thus the target can be sensed. We denote the world frame using w, the body frame using b, and the LiDAR frame using l. In our system, the LiDAR's FOV is attached to the drone's body frame. Transforming the target position ${}^w\xi$ in the world frame to the LiDAR frame, we can derive ${}^l\xi$ as:

$${}^{l}\boldsymbol{\xi} = {}^{b}_{w}\mathbf{R}({}^{b}_{w}\mathbf{q}) ({}^{w}\boldsymbol{\xi} - \mathbf{p}) - {}^{l}_{b}\mathbf{t}, \tag{9}$$

where ${}^b_w \mathbf{q}$ is the rotation quaternion between the world and body frame, ${}^b_w \mathbf{R}$ is the corresponding rotation matrix, and ${}^l_b \mathbf{t}$ is the translation between the LiDAR frame and the body frame. The FOV cost formulation \mathcal{J}_{fov} should consist of vertical and horizontal parts. For omnidirectional sensors, e.g. MID360 LiDAR, only the vertical FOV needs to be regulated to contain the target. We denote the LiDAR's vertical FOV as θ_{vrt} . Given the target at ${}^l \boldsymbol{\xi} = [x_l, y_l, z_l]^T$, we use an auxiliary point \mathbf{p}_c , which is the vertical projection of ${}^l \boldsymbol{\xi}$ on the angle bisector of the vertical FOV, as depicted in Fig.7(c). It can be written as

$$\mathbf{p}_c = [x_l, y_l, \sqrt{x_l^2 + y_l^2} \cdot \tan \theta_{ctr}], \tag{10}$$

where θ_{ctr} is the angle between the bisector of the vertical FOV and the horizon level. As shown in Fig.7(c), to contain the target in vertical FOV, the constraint expects the vertical angle ψ_{vrt} between local vectors ${}^{l}\boldsymbol{\xi}$ and \boldsymbol{p}_{c} to satisfy $\psi_{vrt} < \theta_{vrt}/2$, thus the vertical FOV cost can be formulated as

$$\mathcal{J}_{fov}^{vrt} = \cos\frac{\theta_{vrt}}{2} - \frac{{}^{l}\boldsymbol{\xi} \cdot \boldsymbol{p}_{c}}{\|{}^{l}\boldsymbol{\xi}\| \|\boldsymbol{p}_{c}\|}, \tag{11}$$

For sensors with conic FOVs, e.g. Avia LiDAR, the horizontal FOV cost should be additionally imposed to make the drone face towards the target. The horizontal angle ψ_{hrz} between the target and the heading axis in Fig.7(d) is expected to be zero. Thus, the horizontal FOV cost can be given as

$$\mathcal{J}_{fov}^{hrz} = 1 - \frac{x_l}{\sqrt{x_l^2 + y_l^2}}. (12)$$

For a FOV that perfectly heads towards the target, this horizontal cost equals zero. It's worth noticing that the drone's position \mathbf{p} and attitude \mathbf{q} in Eq.9 can jointly affect the target

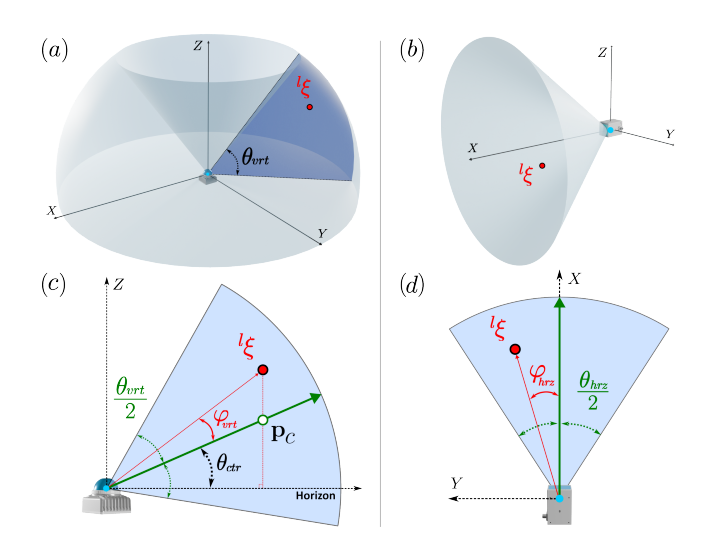


Fig. 7. (a) An overview of the Mid360 FOV. (b) An overview of the Avia FOV. (c) The vertical cross-section of the Mid360 FOV, with the angular bisector marked by the green arrow. To meet the FOV constraint, the angle ψ_{vrt} should be less than $\theta_{vrt}/2$. (d) The horizontal cross-section of the Avia FOV, where the angle ψ_{hrz} is expected to be zero to align with the target.

position ${}^{l}\boldsymbol{\xi}$ in LiDAR frame, hence the proposed \mathcal{J}_{fov} is an SE(3) cost. The gradient w.r.t. \boldsymbol{p} is derived by chain rule as

$$\frac{\partial \mathcal{J}_{fov}}{\partial \mathbf{p}} = \frac{\partial^{l} \boldsymbol{\xi}}{\partial \mathbf{p}} \frac{\partial \mathcal{J}_{fov}}{\partial^{l} \boldsymbol{\xi}}, \quad \frac{\partial^{l} \boldsymbol{\xi}}{\partial \mathbf{p}} = -\frac{b}{w} \mathbf{R}^{T}. \tag{13}$$

The gradient w.r.t. the attitude quaternion can be derived as

$$\frac{\partial \mathcal{J}_{fov}}{\partial_{w}^{b} \mathbf{q}} = \left(\frac{\partial^{l} \boldsymbol{\xi}}{\partial_{w}^{b} \mathbf{q}} \frac{\partial \mathcal{J}_{fov}}{\partial^{l} \boldsymbol{\xi}}\right)^{-1},\tag{14}$$

where $(\cdot)^{-1}$ denotes the inversion of the quaternion, and $\partial^{l} \boldsymbol{\xi}/\partial_{w}^{b} \mathbf{q}$ refers to the Jacobian of a rotated vector w.r.t. the quaternion. To optimize the proposed FOV costs in the drone's flat-output space in the latter Sec.VII, the above gradients should be further transformed to gradients w.r.t. the flat-output variables according to the models in [38].

C. Tracking Distance Cost

A drone is expected to track the target from a proper distance. We expect the Euclidean distance d to satisfy $d_{lb} \le d \le d_{ub}$, where d_{ub} and d_{lb} are the upper and lower bounds of the desired tracking distance. Then the cost is defined as

$$\mathcal{J}_{dis} = \begin{cases} 5 (d_{lb} - d)^3, & d < d_{lb}, \\ 0, & d_{lb} \le d \le d_{ub}, \\ (d - d_{ub})^2 / 2, & d > d_{ub}. \end{cases}$$
(15)

A mild penalty is applied for exceeding d_{ub} due to the LiDAR's long sensing range, but d_{lb} is strictly enforced for the target's safety. Unlike the work [6], [7], we do not rigidly align the altitude of the trackers with the target to meet the FOV requirements. With the costs elaborated in Sec.V-B, the drones can flexibly adjust their altitude according to the needs.

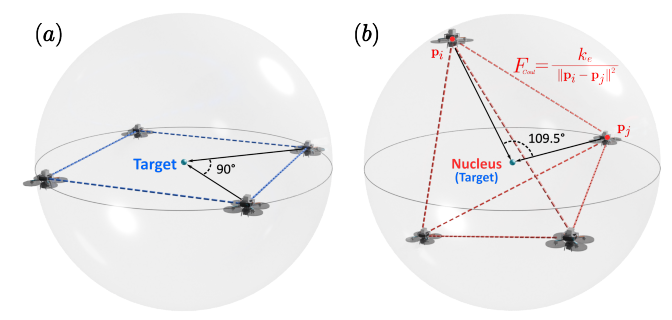


Fig. 8. Distributions of a four-drone swarm on a sphere centered at the target. (a) Conventional 2-D equidistant distribution that confines all drones in a plane. (b) The 3-D uniform encirclement distribution. Surrounding the target as a nucleus, the drones are modeled as electrons repelling each other with Coulomb's forces F_{Coul} , forming an optimal tetrahedral configuration to minimize total electrostatic potential energy.

D. Teammate Occlusion Cost

To enforce teammate occlusion avoidance, trackers must maintain a minimum angular clearance θ_c from each other relative to the target, ensuring the LOS between the tracker and the target is not blocked by teammates. Let η_j denotes the cosine value of the angular distance between teammate j and the ego drone at \mathbf{p}_j , we have

$$\eta_j = \frac{(\mathbf{p}_i - \boldsymbol{\xi}) \cdot (\mathbf{p}_j - \boldsymbol{\xi})}{\|\mathbf{p}_i - \boldsymbol{\xi}\| \|\mathbf{p}_j - \boldsymbol{\xi}\|}.$$
 (16)

When the angular distance occlusion clearance θ_c is violated, *i.e.* $\eta_c > \cos \theta_c$, we impose a occlusion cost term to repulse the tracker away from the teammate j, then \mathcal{J}_{toc} denotes the total collection of the costs on all other teammate drones:

$$\mathcal{J}_{toc} = \sum_{j \neq i}^{N} (\eta_j - \cos \theta_c)^3. \tag{17}$$

The gradients can be easily derived by differentiating Eq.16.

E. Swarm Distribution Cost

In addition to keeping the minimum teammate angular clearance θ_c , the trackers are also expected to achieve uniform multidirectional target coverage in three-dimensional space. The 3-D equidistant encirclement distribution serves two key purposes. Firstly, it allows the swarm to make full use of the vicinity around the target, providing each tracker with the largest angular space to respond to any adverse situations like occlusions or collisions. Secondly, for a swarm tracking system using LiDAR sensors, this strategy can maximize the diversity of target measurement angles, thus the whole swarm can obtain a more complete point cloud of the target for further target state estimation with multi-source fusion. Although for the two-dimensional space, the maximum evenly-spaced angular distance for a swarm of N drones is clearly $2\pi/N$, the same problem in 3-D space is nontrivial. In this context, we introduce a new formulation for the 3-D scenario.

Inspired by the famous Thomson problem [39], we notice that our desired equidistant target encirclement formation resembles the geometry of the optimal configuration described in this problem. The Thomson problem is to determine the

minimum electrostatic potential energy configuration of N electrons constrained on the surface of a unit sphere that repel each other with a Coulomb force, which results in a spatial distribution that exhibits our desired distancing feature. Thus, we transform the initial distribution requirement into the goal of minimizing the total electrostatic potential energy of the swarm. We adopt a logarithmic variant of the original Thomson problem as our cost formulation, which is from the 7th of the eighteen unsolved mathematics problems proposed by Steve Smale - "Distribution of points on the 2-sphere" [40]. The distribution cost for the i^{th} drone is then designed as

$$\mathcal{J}_{frm} = \sum_{j \neq i}^{N} k_e \log \frac{1}{\|\mathbf{p}_i - \mathbf{p}_j\|},$$
 (18)

where k_e is an energy constant. A uniform multidirectional distribution could minimize this logarithmic potential energy objective. Fig.8 illustrates the model and compares the proposed 3-D distribution with the conventional planar formation. Compared to the 2-D square formation, the proposed distribution achieves a 109.5° angle between teammate lines of sight, offering greater angular space for each tracker and increased diversity in viewing angles. This proposed cost describes the ideal distribution. However, in practical tracking, visibility requirements, including FOV compliance, must be prioritized. The FOV configurations in the swarm may not always allow for achieving the ideal distribution, but the planner strives to optimize the distribution cost within the FOV constraints.

F. Other Costs

Other costs serve as the basic requirements for safe swarm navigation. Safe flight corridors are employed for obstacle avoidance. The trajectory of each tracker should be constrained in the polyhedral safe corridors. The formulation is given as

$$\mathcal{J}_{obs} = \mathbf{A}_c \, \mathbf{p} - b_c, \tag{19}$$

where A_c and b_c are from the \mathcal{H} -representation of corridors. For dynamic Feasibility, we limit the maximum amplitudes of the tracker's velocity, acceleration, and angular velocity to keep the trajectory executable. The velocity cost is given as

$$\mathcal{J}_{dyn}^{vel} = \|\mathbf{v}\|^2 - v_{max}^2, \tag{20}$$

where ${\bf v}$ denotes the velocity and v_{max} denotes the upper bounds. The costs for acceleration and angular velocity are in the same form. To enforce inter-vehicle collision avoidance, we expect each drone to maintain a distance clearance r_s to all other teammates. For the ego drone at ${\bf p}_i$ and one teammate drone at ${\bf p}_i$, the reciprocal clearance cost is given as

$$\mathcal{J}_{swm}^{j} = \max\{r_s^2 - \|\mathbf{p}_i - \mathbf{p}_j\|^2, 0\}.$$
 (21)

Then the total clearance cost \mathcal{J}_{swm} for ego drone i is the sum of the costs on all other teammate drones.

VI. KINODYNAMIC SEARCHING

Our kinodynamic front-end generates a reference path by expanding motion primitives in a discretized control space. Unlike traditional hybrid A* searchers [41]–[43] that prioritize

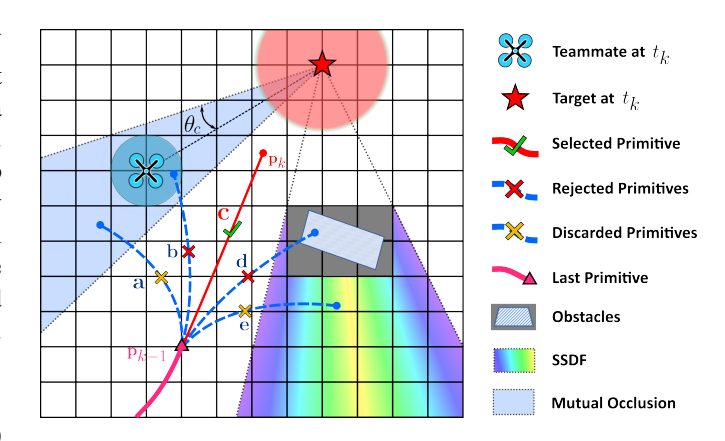


Fig. 9. An illustration of the primitive selection mechanism in our task-oriented kinodynamic searcher. Primitives **b** and **d** are rejected by inter-UAV safety check and obstacle check, respectively. Primitives **a** and **e** are penalized due to inter-UAV occlusion and environmental occlusion, respectively.

minimizing control effort along the path, our method scores each primitive based on the tracking performance metrics defined in the previous section, ensuring high consistency between the front-end and the overall task objectives.

A. Primitive Expansion and Rejection

The state $\mathbf{x} \in \mathbb{R}^6$ of the tracker drone includes its position $\mathbf{p} = [p_x, p_y, p_z]^T$ and velocity $\mathbf{v} = [v_x, v_y, v_z]^T$. Acceleration is used as the control input for each dimension, and the input space is discretized as $\mathbf{u}_d = \{-a_{max}, 0, a_{max}\}$, where a_{max} is the acceleration limit. As mentioned in Sec.IV-D, a prediction module interpolates future target positions based on the time step δT and prediction horizon T_p , represented by Eq.6. In the front-end, motion primitives for the tracker drone are expanded directly using the prediction interval δT , ensuring that the timestamp t_k of each new node \mathbf{x}_k aligns with the stamp of target prediction ξ_k . Motion primitive expansion follows the double-integrator dynamics. To meet the task requirements and accelerate the searching, we design pruning strategies to reject the infeasible nodes in the primitive expansion process timely. After each expansion step, all resultant nodes are checked in terms of obstacle avoidance, dynamic feasibility, and intervehicle safety. For mutual collision avoidance, we first query the current positions of teammate drones on the broadcast trajectories. Then a node is considered safe if the distances between the node and all its teammates are larger than a clearance r_s . Fig.9 shows examples of primitive rejection.

B. Cost Functions

After the expansion and rejection process, every remaining node \mathbf{x}_k is assigned a cost g_k as a coarse assessment of its tracking quality with target $\boldsymbol{\xi}_k$. We evaluate the performance of each node in terms of obstacle occlusion \mathcal{J}_{vis} , tracking distance \mathcal{J}_{dis} , teammate occlusion \mathcal{J}_{toc} , and swarm distribution \mathcal{J}_{frm} . In the existing works [7], [23], the searcher penalizes the obstacle occlusion using a measure of voxel occupancy along the LOS between target and tracker, which is not yet a reasonable quantification for occlusion. The severity

of occlusion should be defined by the difficulty of the tracker escaping from the invisible area, which can be described by the angular distance to the closest visibility boundary in SSDFs. Thus, we use the cost \mathcal{J}_{vis} to penalize the occlusion. Synthesizing all the terms, we have the node cost g_k as

$$g_n = [\mathcal{J}_{vis}, \mathcal{J}_{dis}, \mathcal{J}_{toc}, \mathcal{J}_{frm}] \cdot w, \tag{22}$$

where w is the weight vector to trade off cost priorities. In our planner, safety constraints are prioritized first, followed by LOS visibility requirements, and lastly swarm distribution considerations. The searching terminates when one primitive reaches the target prediction horizon T_p , determining the final path. We utilize the remaining expansion time $h_n = T_p - t_k$ as a heuristic function to speed up the searching process.

C. Flight Corridor Generation

After finding the minimum-cost path, an efficient method in [44] is applied to generate a safe flight corridor of connected polyhedra along the path, each polyhedron is denoted as

$$\mathcal{P} = \{ x \in \mathbb{R}^3 \mid \mathbf{A}_c \, x \le b_c \}. \tag{23}$$

The corridors will be used as the safe constraints.

VII. SPATIOTEMPORAL TRAJECTORY OPTIMIZATION

A. Trajectory Optimization Problem Formulation

In this work, we use the MINCO representation [45], a minimum control effort polynomial trajectory class to conduct spatiotemporal deformation of the flat-output trajectory

$$\mathfrak{T}_{MINCO} = \{ \mathbf{p}(t) : [0, T_{\Sigma}] \mapsto \mathbb{R}^{m} | \mathbf{c} = \mathcal{C}(\boldsymbol{\varrho}, \mathbf{T}),$$

$$\boldsymbol{\varrho} \in \mathbb{R}^{m(M-1)}, \mathbf{T} \in \mathbb{R}^{M}_{>0} \},$$
(24)

where $\mathbf{c}=(\mathbf{c}_1^T,\cdots,\mathbf{c}_M^T)^T$ is the polynomial coefficient, $\boldsymbol{\varrho}=(\varrho_1,\cdots,\varrho_{M-1})$ the intermediate points between trajectory pieces, $\mathbf{T}=(T_1,\cdots,T_M)^T$ the time vector, $\mathcal{C}(\boldsymbol{\varrho},\mathbf{T})$ is the linear-complexity parameter mapping from [45], and T_Σ is the total trajectory duration. For the s-order \mathfrak{T}_{MINCO}^s , a m-dimensional M-piece trajectory $\mathbf{p}(t)$ is defined as $\mathbf{p}(t)=\mathbf{p}_i(t-t_{i-1}), \quad \forall t\in[t_{i-1},t_i),$ and the i^{th} piece trajectory is represented by a (2s-1)-degree polynomial $\mathbf{p}_i(t)=\mathbf{c}_i^T\boldsymbol{\beta}(t), \quad \forall t\in[0,T_i].$ MINCO trajectories are all compactly parameterized by $\boldsymbol{\varrho}$ and \mathbf{T} . With mapping $\mathcal{C}(\boldsymbol{\varrho},\mathbf{T})$, the cost of the polynomial trajectories in \mathfrak{T}_{MINCO} can be evaluated by $\boldsymbol{\varrho}$ and \mathbf{T} by $\mathcal{J}(\boldsymbol{\varrho},\mathbf{T})=\mathcal{F}(\mathbf{c},\mathbf{T})=\mathcal{F}(\mathcal{C}(\boldsymbol{\varrho},\mathbf{T}),\mathbf{T}).$ Thus, we can conduct trajectory optimization over objective \mathcal{J} using the gradients $\partial \mathcal{J}/\partial \boldsymbol{\varrho}$ and $\partial \mathcal{J}/\partial \mathbf{T}$, which are propagated from gradients $\partial \mathcal{F}/\partial \mathbf{c}$ and $\partial \mathcal{F}/\partial \mathbf{T}$ accordingly.

With \mathfrak{T}^s_{MINCO} , the trajectory optimization problem can be formulated as follows:

$$\min_{\boldsymbol{\varrho}, \mathbf{T}} \mathcal{J}_E = \int_0^{T_{\Sigma}} \|\mathbf{p}^{(s)}(t)\|^2 dt$$
 (25a)

s.t.
$$T_{\Sigma} = T_p$$
, (25b)

$$\mathcal{G}(\mathbf{p}^{[s-1]}(t)) \le \mathbf{0}, \, \forall t \in [0, T_{\Sigma}], \tag{25c}$$

$$\mathcal{H}(\mathbf{p}^{[s-1]}(t)) \le \mathbf{0}, \, \forall t \in \mathcal{T},$$
 (25d)

where T_p is the target prediction horizon. Cost function Eq.25a is the control effort objective. In Eq.25b, the total trajectory

duration T_{Σ} is set equal to T_p , meaning the tracking trajectory is generated only up to the target prediction horizon. This ensures that the trajectory's terminal state at T_{Σ} can correspond to the target's last predicted position. Thus, the trajectory duration is fixed to T_p using the equality constraint. Eq.25c defines inequality constraints enforced continuously over the entire duration, and Eq.25d are the inequality constraints that are discretely enforced at the target's predicted timestamps \mathcal{T} .

In typical hierarchical tracking planners, the terminal position of the trajectory is set to the last state of the front-path, and the terminal velocity is set to the target velocity to keep up with the target. In this work, we fix solely the terminal velocity and rather treat the other terminal states as decision variables in optimization to compute the optimal states. We have some tracking constraints for the unfixed terminal states, which are included in Eq.25d with $t=T_{\Sigma}$.

To conveniently solve the continuous constrained optimization problem, we transform it into an unconstrained optimization. The temporal constraint Eq.25b can be eliminated by variable substitution. The inequality constraints Eq.25c and Eq.25d can be converted into penalty terms using the penalty method. Then the original problem Eq.25 is converted into the following unconstrained format:

$$\min_{\mathbf{g}, \mathbf{T}} \mathcal{J}_E + \int_0^{T_{\Sigma}} \mathcal{J}_{\mathcal{G}} dt + \sum_{t \in \mathcal{T}} \mathcal{J}_{\mathcal{H}}, \tag{26}$$

where $\mathcal{J}_{\mathcal{G}}$ is the penalty function of the continuous constraints Eq.25c, and $\mathcal{J}_{\mathcal{H}}$ is the penalty function of the discrete constraints Eq.25d. In this work, we adopt $\mathfrak{T}_{MINCO}^{s=4}$ trajectories (i.e. 7-degree polynomials) to represent the drone position. For cases requiring yaw planning, such as the Avia tracker, a $\mathfrak{T}_{MINCO}^{s=2}$ trajectory (i.e. a 3-degree polynomial) is used to represent the drone's yaw angle. The position and yaw trajectories are jointly optimized upon the cost objectives in Eq.26. The positional trajectories are initialized using the path obtained from the front-end kinodynamic searching, the yaw angles are initially set to head toward the target positions, and the initial piece duration $T_i = T_p/M$.

B. Continuous Relative-time Penalty

Denote the continuous penalty term (the second term) in Eq.26 as \mathcal{J}_C . These penalty functions are evaluated on relative times along the whole trajectory. To efficiently compute violations, we transform the continuous constraints into finite ones using constraint transcription [46]. Penalties $\mathcal{J}_{\mathcal{G}}$ are numerically integrated by sampling all the pieces of the trajectory evenly with time step T_i/κ_i , where κ_i denotes the sample number of the i^{th} piece. So we have

$$\mathcal{J}_C = \int_0^{T_{\Sigma}} \mathcal{J}_{\mathcal{G}} dt = \sum_i^M \frac{T_i}{\kappa_i} \sum_{j=0}^{\kappa_i} \bar{\omega}_j \mathcal{J}_{\mathcal{G}}(t_j), \qquad (27)$$

where $t_j=(j/\kappa_i)T_i$ refers to the relative time sampled on the i^{th} piece. Integral coefficients $(\bar{\omega}_0,\bar{\omega}_1,\cdots,\bar{\omega}_{\kappa_i-1},\bar{\omega}_{\kappa_i})=(1/2,1,\cdots,1,1/2)$ follow the trapezoidal rule. The continuous penalties include obstacle avoidance, dynamic feasibility and swarm reciprocal clearance, which can be listed as

$$\mathcal{J}_{\mathcal{G}} = \lambda_{\mathcal{G}} \left[\mathcal{J}_{obs}, \mathcal{J}_{dyn}, \mathcal{J}_{swm} \right]^{T}, \tag{28}$$

where $\lambda_{\mathcal{G}}$ is the penalty weight vector. These constraints can be divided into two categories: one is at the single-UAV navigation level, and the other is for the swarming.

1) Single-UAV Navigation Constraints: The constraints for obstacle avoidance \mathcal{J}_{obs} and dynamic feasibility \mathcal{J}_{dyn} act as the basic constraints for drone navigation. In this category, $\mathcal{J}_{\mathcal{G}}$ is a function of ego states $\mathbf{p}_i^{[s-1]}(t_j)$, thus we can derive the gradients of \mathcal{J}_C in Eq.27 w.r.t. \mathbf{c}_i and T_i by chain rule

$$\frac{\partial \mathcal{J}_C}{\partial \mathbf{c}_i} = \frac{\partial \mathcal{J}_C}{\partial \mathcal{J}_C} \frac{\partial \mathcal{J}_G}{\partial \mathbf{c}_i},\tag{29}$$

$$\frac{\partial \mathcal{J}_C}{\partial T_i} = \frac{\mathcal{J}_C}{T_i} + \frac{\partial \mathcal{J}_C}{\partial \mathcal{J}_g} \frac{\partial \mathcal{J}_g}{\partial t_i} \frac{\partial t_j}{\partial T_i},\tag{30}$$

where the gradients

$$\frac{\partial \mathcal{J}_{\mathcal{G}}}{\partial \mathbf{c}_{i}} = \sum_{k=0}^{s-1} \frac{\partial \mathbf{p}_{i}^{(k)}}{\partial \mathbf{c}_{i}} \frac{\partial \mathcal{J}_{\mathcal{G}}}{\partial \mathbf{p}_{i}^{(k)}} = \sum_{k=0}^{s-1} \beta^{(k)}(t_{j}) \frac{\partial \mathcal{J}_{\mathcal{G}}}{\partial \mathbf{p}_{i}^{(k)}}, \tag{31}$$

$$\frac{\partial \mathcal{J}_{\mathcal{G}}}{\partial t_{j}} = \sum_{k=0}^{s-1} \frac{\partial \mathbf{p}_{i}^{(k)}}{\partial t_{j}} \frac{\partial \mathcal{J}_{\mathcal{G}}}{\partial \mathbf{p}_{i}^{(k)}} = \sum_{k=0}^{s-1} \mathbf{p}_{i}^{(k+1)} \frac{\partial \mathcal{J}_{\mathcal{G}}}{\partial \mathbf{p}_{i}^{(k)}}, \quad (32)$$

and $\partial t_j/\partial T_i = j/\kappa_i$. The derivatives $\partial \mathcal{J}_{\mathcal{G}}/\partial \mathbf{p}_i^{(k)}$ are determined by the formulations of the constraints.

2) Swarm Navigation Constraints: With the communication network, each drone receives teammates' trajectories to formulate swarm constraints and optimizes its own trajectory accordingly. The constraint of safe clearance \mathcal{J}_{swm} in Eq.21 accounts for the swarm mutual collision avoidance. Unlike the single-UAV constraints, \mathcal{J}_{swm} is not only a function of ego position $\mathbf{p}_i(t_j)$, but also involves the teammates' positions. We need to use the relative time $t_j=(j/\kappa_i)T_i$ for the ego trajectory and the corresponding absolute timestamp τ to query the teammate positions on received trajectories, where $\tau=\sum_{l=1}^{i-1}T_l+(j/\kappa_i)T_i$. For a swarm of N drones, let $\mathbf{p}_\phi(\tau)$ denote the trajectory from the teammate drone ϕ and \mathcal{J}_{swm}^ϕ denote the clearance constraint associated with teammate ϕ , then the violation \mathcal{J}_C of this constraint is formulated as

$$\mathcal{J}_C = \sum_{i}^{M} \frac{T_i}{\kappa_i} \sum_{j=0}^{\kappa_i} \bar{\omega}_j \sum_{\phi}^{N} \mathcal{J}_{swm}^{\phi}(\mathbf{p}_i(t_j), \mathbf{p}_{\phi}(\tau)). \tag{33}$$

Note that term τ introduces \mathcal{J}_{swm}^{ϕ} the gradient dependence on its preceding pieces T_l through $\mathbf{p}_{\phi}(\tau)$. So temporal gradient

$$\frac{\partial \mathcal{J}_{swm}^{\phi}}{\partial T_{l}} = \frac{\partial t_{j}}{\partial T_{l}} \frac{\partial \mathbf{p}_{i}}{\partial t_{i}} \frac{\partial \mathcal{J}_{swm}^{\phi}}{\partial \mathbf{p}_{i}} + \frac{\partial \tau}{\partial T_{l}} \frac{\partial \mathbf{p}_{\phi}}{\partial \tau} \frac{\partial \mathcal{J}_{swm}^{\phi}}{\partial \mathbf{p}_{\perp}}, \quad (34)$$

$$\frac{\partial t_j}{\partial T_l} = \begin{cases} \frac{j}{\kappa_i}, & l = i, \\ 0, & l < i, \end{cases} \frac{\partial \tau}{\partial T_l} = \begin{cases} \frac{j}{\kappa_i}, & l = i, \\ 1, & l < i. \end{cases}$$
(35)

Other components of gradients $\partial \mathcal{J}_C/\partial \mathbf{c}_i$ and $\partial \mathcal{J}_C/\partial T_i$ are in the same forms as the ones in the single-UAV constraints.

C. Discrete Absolute-time Penalty

Denote the discrete penalty (the third term) in Eq.26 as \mathcal{J}_D . To impose these penalties related to target tracking requirements, constraint violation is evaluated at absolute time t_k , which is the k^{th} timestamp of the target prediction, with the

corresponding penalty assessed using the k^{th} target position of the prediction series. So we have

$$\mathcal{J}_D = \sum_{k=1}^{N_p} \delta T \cdot \mathcal{J}_{\mathcal{H}}(t_k), \tag{36}$$

where δT and N_p are the time interval and total number of predictions. $\mathcal{J}_{\mathcal{H}}$ includes all the tracking-related constraints introduced in Sec.V-A to Sec.V-E, which can be listed as

$$\mathcal{J}_{\mathcal{H}} = \lambda_{\mathcal{H}} \left[\mathcal{J}_{vis}, \mathcal{J}_{fov}, \mathcal{J}_{dis}, \mathcal{J}_{toc}, \mathcal{J}_{frm} \right]^{T}, \tag{37}$$

where $\lambda_{\mathcal{H}}$ is the penalty weight vector. These tracking constraints can be divided into two categories: one is at the single-UAV level, and the other is for swarm cooperation.

1) Single-UAV Tracking Constraints: In this category, constraints \mathcal{J}_{vis} , \mathcal{J}_{fov} , and \mathcal{J}_{dis} are associated with the tracking performance from the single-UAV aspect. Thus $\mathcal{J}_{\mathcal{H}}$ is a function of solely ego state $\mathbf{p}_i^{[s-1]}(t_k)$. Assume that t_k is located on the i^{th} piece of the trajectory, then the corresponding relative time t_r of t_k on the i^{th} piece becomes $t_r = t_k - \sum_{l=1}^{i-1} T_l$, where T_l denotes the preceding piece duration. Note that the formulation of t here brings in the gradient dependence on all T_l with $1 \leq l \leq i$. Thus, the gradients of \mathcal{J}_D are derived as

$$\frac{\partial \mathcal{J}_D}{\partial \mathbf{c}_i} = \frac{\partial \mathcal{J}_H}{\partial \mathbf{c}_i} \frac{\partial \mathcal{J}_D}{\partial \mathcal{J}_H}, \ \frac{\partial \mathcal{J}_D}{\partial T_l} = \frac{\partial \mathcal{J}_H}{\partial T_l} \frac{\partial \mathcal{J}_D}{\partial \mathcal{J}_H}, \tag{38}$$

$$\frac{\partial \mathcal{J}_{\mathcal{H}}}{\partial \mathbf{c}_{i}} = \sum_{k=0}^{s-1} \frac{\partial \mathbf{p}_{i}^{(k)}}{\partial \mathbf{c}_{i}} \frac{\partial \mathcal{J}_{\mathcal{H}}}{\partial \mathbf{p}_{i}^{(k)}} = \sum_{k=0}^{s-1} \beta^{(k)}(t_{r}) \frac{\partial \mathcal{J}_{\mathcal{H}}}{\partial \mathbf{p}_{i}^{(k)}}, \quad (39)$$

$$\frac{\partial \mathcal{J}_{\mathcal{H}}}{\partial T_{l}} = \frac{\partial t_{r}}{\partial T_{l}} \sum_{k=0}^{s-1} \mathbf{p}_{i}^{(k+1)} \frac{\partial \mathcal{J}_{\mathcal{H}}}{\partial \mathbf{p}_{i}^{(k)}}, \frac{\partial t_{r}}{\partial T_{l}} = \begin{cases} 0, & l = i, \\ -1, & l < i, \end{cases}$$
(40)

The derivatives $\partial \mathcal{J}_{\mathcal{H}}/\partial \mathbf{p}_i^{(k)}$ are determined by the specific formulations of the constraints.

2) Swarm Tracking Constraints: The constraints \mathcal{J}_{toc} and \mathcal{J}_{frm} are designed to coordinate the swarm during the tracking process. Unlike the continuous reciprocal collision constraint \mathcal{J}_{swm} , the teammate position $\mathbf{p}_{\phi}(t_k)$ in \mathcal{J}_{toc} and \mathcal{J}_{frm} produces no extra gradients. It is because both teammate and ego trajectories in the discrete constraints are queried using the same fixed absolute time t_k , thus the teammate position $\mathbf{p}_{\phi}(t_k)$ is a constant throughout the optimization iterations. Therefore, all the gradients of $\mathcal{J}_{\mathcal{H}}$ have identical forms as the ones in single-UAV tracking constraints.

D. Temporal Constraint Elimination

We use the variable substitution from [45] to eliminate the temporal equality constraint of Eq.25b. Denote by $\iota = (\iota_1,...,\iota_M) \in \mathbb{R}^M$ the new temporal variables to be optimized. The transformation is given by the map below for 1 < i < M

$$T_i = \frac{e^{\iota_i}}{1 + \sum_{j=1}^{M-1} e^{\iota_j}} T_p, \ T_M = T_p - \sum_{j=1}^{M-1} T_j.$$
 (41)

With the new decision variables ι , the temporal constraint can be satisfied by default. As the total duration T_{Σ} is fixed to T_p , the constraints $\mathcal{H}(\mathbf{p}^{[s-1]}(t))$ in Eq.25d exerted on the terminal

states at $t=T_{\Sigma}$ do not have dependence on time anymore (since T_p is a constant). Thus, the terminal penalties only have dependence on the spatial variation of the terminal states, and the temporal gradients at T_{Σ} are zero.

VIII. SIMULATION AND BENCHMARK

In this section, we conduct extensive comparative studies to validate the performance of our swarm tracking planner. All simulations in this section are run on an Intel Core i9-12900K CPU with an NVIDIA GeForce RTX 3070Ti GPU.

A. General Benchmark of Swarm Tracking Planners

To demonstrate the advantages of our method, benchmark comparisons are conducted against other cutting-edge swarm tracking works. The proposed planner is compared with Zhou's work [6], Ho's work [23], and Yin's work [7]. As a baseline method, Zhou's planner [6] utilizes a predefined constant leader-follower formation to track the target. Ho's planner [23] and Yin's planner [7] actively consider the target visibility. Ho *et al.* [23] uses a centralized dynamic programming to search the occlusion-free formation configuration for the swarm. Yin *et al.* [7] build the planar visible sectors to avoid environmental occlusion. Each planner is fine-tuned to its best tracking performance.

To compare the planners fairly, we simulate four swarms, each with four trackers, chasing an identical target drone simultaneously. Each swarm runs one benchmarked planner, tested on two dense random maps with different obstacle types: Forest (Fig.10(a)) and Walls (Fig.10(b)). Since the target maneuverability directly influences tracking difficulty, we implement and test two target velocity modes: slow (1.0m/s)and fast (2.5m/s). Moreover, to reflect the impact of FOV shapes on swarm tracking, we design two swarm configurations with varied FOV settings. The first configuration (Swarm Configuration A) comprises four drones equipped with regular upward-facing Mid360 LiDARs, as shown in Fig.10(c). The second configuration (Swarm Configuration B) integrates two drones with the upward-facing LiDARs and two drones with downward-facing Mid360 LiDARs, as shown in Fig.10(d). Testing is limited to horizontally omnidirectional FOVs due to the lack of yaw planning in the other benchmarked planners.

The tracking performance is evaluated over four metrics from [7]: average target visibility (ϑ_{avg}) , worst-case visibility (ϑ_{wrst}) , full-visibility time ratio (γ_{vis}) , and average tracking distance (d_{avg}) . A tracker is considered losing the target if the LOS is blocked by obstacles/teammates, or the target exits the FOV, or the tracking distance becomes too close. The swarm visibility $\vartheta(t)$ is defined as the count of trackers that are not losing the target at time t. For a tracking task with duration T_b , the average visibility ϑ_{avg} is calculated by

$$\vartheta_{avg} = \frac{1}{T_b} \int_0^{T_b} \vartheta(t) dt. \tag{42}$$

Practically, this metric ϑ_{avg} is numerically integrated with a 0.05-second sampling interval. The metric ϑ_{wrst} represents the lowest swarm visibility over the task. Let T_{vis} denote the total time duration in which the target is fully visible to all trackers;

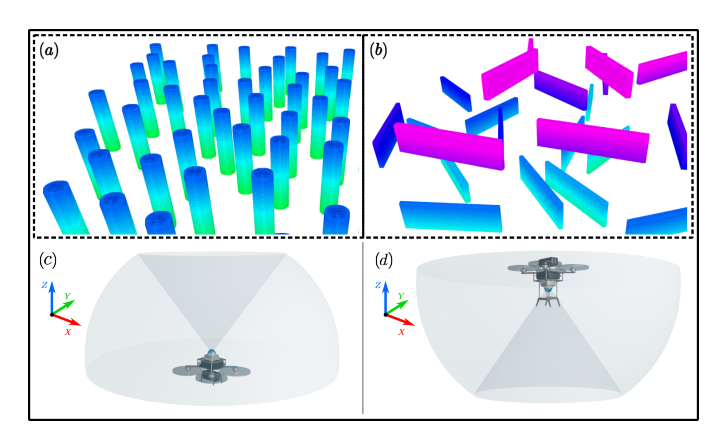


Fig. 10. (a) The Forest map used in the general benchmark. (b) The Walls map. (c) An illustration of the tracker drone with a regular upward-facing Mid360 LiDAR unit. (d) An illustration of the tracker drone with an inverted downward-facing Mid360 LiDAR unit.

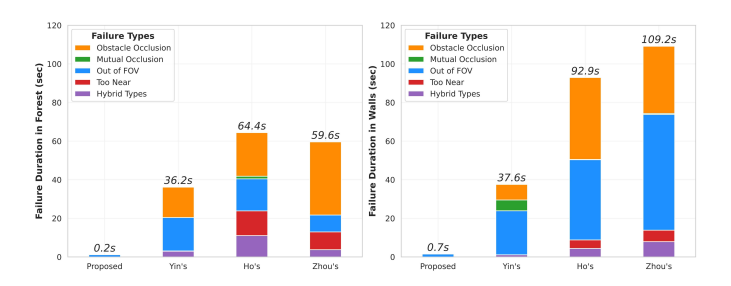


Fig. 11. Histograms of swarm-wide cumulative target loss duration with breakdowns by failure types (target velocity = 2.5m/s). **Left**: Histograms for the Forest map; **Right**: Histograms for the Walls map.

then metric γ_{vis} refers to the ratio of T_{vis} to T_b . The tracking distance d_{avg} is averaged in the same manner as ϑ_{avg} . Each test case undergoes four independent trials, and the trial with the highest ϑ_{avg} is selected as the benchmark.

The results are summarized in Tab.I. Our method outperforms other works in terms of ϑ_{avq} , ϑ_{wst} , and γ_{vis} in all cases with satisfactory distances d_{avq} . Notably, Zhou's and Ho's methods occasionally yield zero swarm visibility in worst-case scenarios, which could be fatal in real-world tracking applications. Significant performance degradation is observed in the three benchmarked planners when the target speed increases from 1.0m/s to 2.5m/s. Fig.11 presents the cumulative target loss duration across all swarm trackers in the high-speed scenarios, along with its breakdown by specific failure reasons. The results in Tab.I also indicate worse tracking performance in the Walls environment compared to the Forest map, attributed to challenges such as difficult occlusion recovery from wall-shaped structures, increased vertical obstacle complexity, and greater target velocity fluctuations in the scenario. Importantly, our planner maintains nearcomplete swarm visibility (> 99%) across all test conditions, demonstrating its robust adaptability to different environments, varied FOV settings, and fast target dynamics.

TABLE I
VISIBILITY-AWARE SWARM TRACKING BENCHMARK RESULTS

	Configuration	Swarm Configuration A				Swarm Configuration B			
Scenario	Metric Method	$oldsymbol{artheta}_{avg}$	$oldsymbol{artheta}_{wrst}$	$oldsymbol{\gamma_{vis}}(\%)$	$d_{avg}(m)$	$oldsymbol{artheta}{avg}$	$oldsymbol{artheta}_{wrst}$	$oldsymbol{\gamma}_{vis}(\%)$	$d_{avg}(m)$
	Zhou et al. [6]	3.757	2.0	77.407	2.025	3.732	2.0	75.388	2.018
Forest	Ho et al. [23]	3.821	2.0	83.509	1.952	3.780	2.0	81.109	1.925
(1.0m/s)	Yin et al. [7]	3.932	3.0	93.231	1.891	3.904	2.0	90.599	1.877
	Proposed	4.000	4.0	100.000	2.016	4.000	4.0	100.000	2.012
	Zhou et al. [6]	3.535	0.0	62.323	2.052	3.538	0.0	60.786	2.035
Forest	Ho et al. [23]	3.475	1.0	61.774	1.938	3.511	1.0	62.096	1.880
(2.5m/s)	Yin et al. [7]	3.773	2.0	80.298	1.992	3.666	1.0	73.652	2.006
	Proposed	3.997	3.0	99.686	1.970	4.000	4.0	100.000	1.980
	Zhou et al. [6]	3.433	1.0	64.613	2.030	3.430	1.0	61.069	2.020
Walls	Ho et al. [23]	3.514	1.0	67.214	1.988	3.514	1.0	67.214	1.988
(1.0m/s)	Yin et al. [7]	3.919	3.0	91.917	1.925	3.874	2.0	88.274	1.905
	Proposed	4.000	4.0	100.000	1.926	4.000	4.0	100.000	1.976
	Zhou et al. [6]	3.182	0.0	53.383	2.072	3.194	1.0	49.590	2.101
Walls	Ho et al. [23]	3.252	1.0	50.037	1.955	3.365	0.0	58.451	1.962
(2.5 m/s)	Yin et al. [7]	3.758	1.0	80.223	1.950	3.684	1.0	75.577	1.940
	Proposed	3.993	3.0	99.331	1.932	3.996	3.0	99.628	1.951

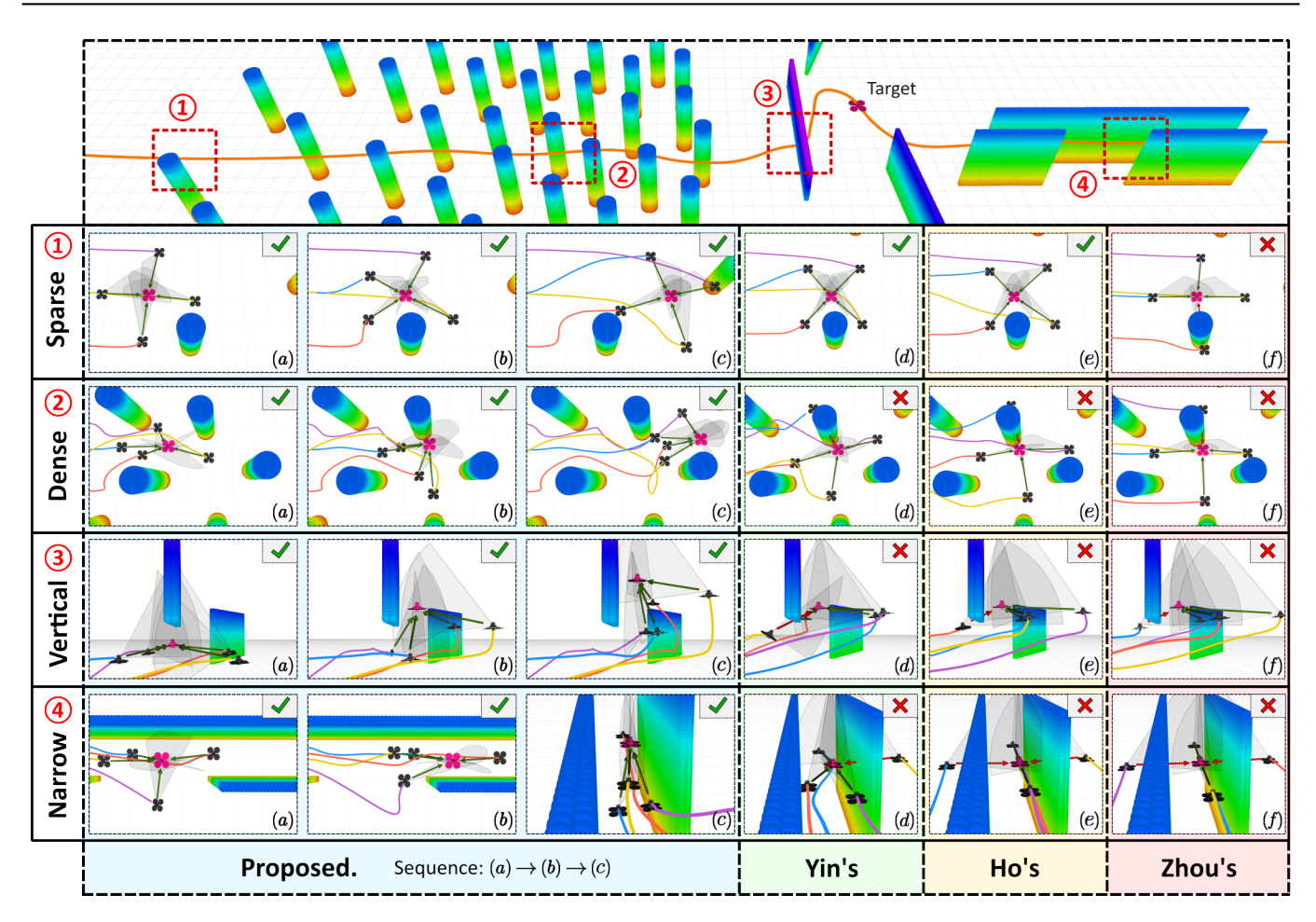


Fig. 12. Tracking performance in the case study. **Top**: The orange trajectory is executed by the target. Four areas, ①-④, are highlighted, featuring *Sparse* clutter, *Dense* clutter, *Vertical* structures, and *Narrow* passages. **Rows** ①-④: Snapshots of swarm tracking in areas ①-④. Subfigures (a)-(c) show the swarm behaviour of the proposed method. Benchmark results are shown in subfigures (d)-(f). The LiDAR FOVs' vertical cross-sections are depicted as gray sectors.

B. Case Study of Swarm Tracking Planners

This section presents a case study showcasing the performance of the compared methods. We establish a representative

test map containing diverse obstacle conditions (*Sparse* clutter, *Dense* clutter, *Vertical* structures, and *Narrow* passages). For each method, we simulate a four-drone swarm equipped with

upward-facing LiDARs tracking the target through the heterogeneous environment. Fig.12 illustrates the test map and the tracking behaviors. The visible Lines of Sight are marked by the green arrows connecting the trackers and the target, whereas red arrows indicate the visibility loss.

In the Sparse area, Zhou's method has visibility loss due to its simple constant leader-follower formation strategy. Other methods manage to avoid the occlusion by adjusting the swarm. In the *Dense* area, only the proposed method maintains full swarm visibility. Ho's method loses visibility as it cannot find feasible occlusion-free configurations for its rigid square formation under dense clutter. Yin's work has occlusion due to the insufficient agility of its 2-D costs. The proposed planner ensures flexible occlusion-free swarm navigation in tight spaces with FOV compliance. When encountering the Vertical obstacles, Yin's planner fails to timely avoid the occlusion along the Z-axis, as its visible sectors can only consider the 2-D visibility at a certain height. In contrast, our SSDF framework encodes the target visibility in the whole 3-D space, enabling the tracker to adjust LOS promptly against the 3-D occlusion when tracking a vertically moving target. In Narrow passages, the visibility of the other three planners degrades due to the maneuverability limitations imposed by their 2-D motion constraints. Conversely, the proposed method formulates all tracking requisites within a true 3-D framework. This empowers the planner to coordinate the swarm at different heights, adaptively exploiting the vertical space to achieve fullvisibility tracking with strict FOV compliance, even in highly confined scenes.

C. Ablation Study

Ablation studies are conducted to further validate the necessity of the proposed modules and costs for swarm tracking. To verify the kinodynamic front-end's contribution, we replace it with a vanilla A* searcher from [5], designating this variant as **w/o KinoSearch**. We then systematically remove all SSDF-based occlusion avoidance costs throughout the planning pipeline to create the **w/o Visibility** variant, while canceling all equidistant 3-D swarm distribution costs gives the variant **w/o Formation**. Finally, our full **Proposed** planner and Zhou's work [6], as the **Baseline**, are also evaluated for comparison.

All variants are tested in random Forest maps with five different tree density levels, varying from sparse $(1/32\,tree/m^2)$ to dense $(1/9\,tree/m^2)$. Each cylindrical tree obstacle has a height of 4m and a diameter of 1m. In each trial, five trackers with upward-facing Mid360 LiDARs collaborate to pursue a target traversing the map at velocities up to 1.4m/s.

The ablation results are shown in Fig.13, which also depicts the visibility loss duration in the densest map. The **Baseline** method exhibits the largest swarm visibility degradation as obstacle density increases. The A* searching in the variant **w/o KinoSearch** merely minimizes the path distance while disregarding other task requirements, thereby rendering low-performance path topologies that overburden the back-end optimizer. Without the information from SSDFs, the variant **w/o Visibility** becomes highly vulnerable to occlusions. While the variant **w/o Formation** leverages the kinodynamic searcher

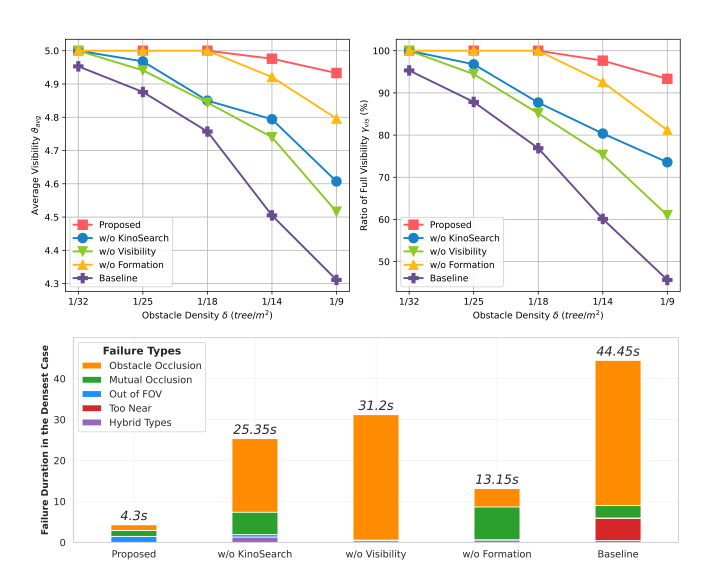


Fig. 13. Ablation study results. **Top-left**: The average visibility (ϑ_{avg}) profiles across all variants. **Top-right**: The full visibility ratio (γ_{vis}) profiles across all variants. **Bottom**: The target loss duration histograms recording the test cases in the densest map $(1/9 \, tree/m^2)$.

and SSDFs to reduce obstacle occlusions, the lack of swarm distribution guidance makes trackers prone to clustering behind the target in highly constrained scenes, inducing the risks of mutual occlusion. In contrast, the **Proposed** employs the distribution costs in both front-end and back-end to effectively mitigate the inter-vehicle interference, hence greatly enhancing the swarm visibility in dense areas. Through component ablation, we validate the contribution of the proposed modules and costs in ensuring the framework's overall performance.

D. Study on Swarm Size

In this section, we conduct a scalability analysis of the proposed planner, investigating the impact of increasing swarm size on both tracking performance and computational overhead. Yin's work, the top performer among the benchmarked methods, serves as the baseline. Five swarms of 2 to 10 drones are simulated, with each swarm maintaining a balanced sensor setup: half the drones are equipped with upward Mid360 LiDARs and half with downward Mid360 LiDARs. Subfigures (a)-(d) in Fig. 14 visualize the tracking behaviors of the eightdrone swarm, while (e)-(f) record the full-visibility time ratio throughout the mission and the average runtime per replanning cycle. As depicted in Fig.14(a)-(b), with the proposed FOV costs and spatial distribution costs, our planner can coordinate the swarm to exploit vertical airspace while ensuring strict FOV compliance. The drones adaptively configure into a 3-D polyhedral formation where downward-facing drones establish the upper facet and upward-facing drones form the lower facet. This distribution optimally leverages the free space for occlusion-averse maneuvering. Conversely, Yin's method exhibits inefficient spatial utilization and large visibility degradation as the swarm size scales up, which is due to its 2-D motion constraints and the lack of FOV-aware planning. In Fig.14(f), both methods maintain a manageable average

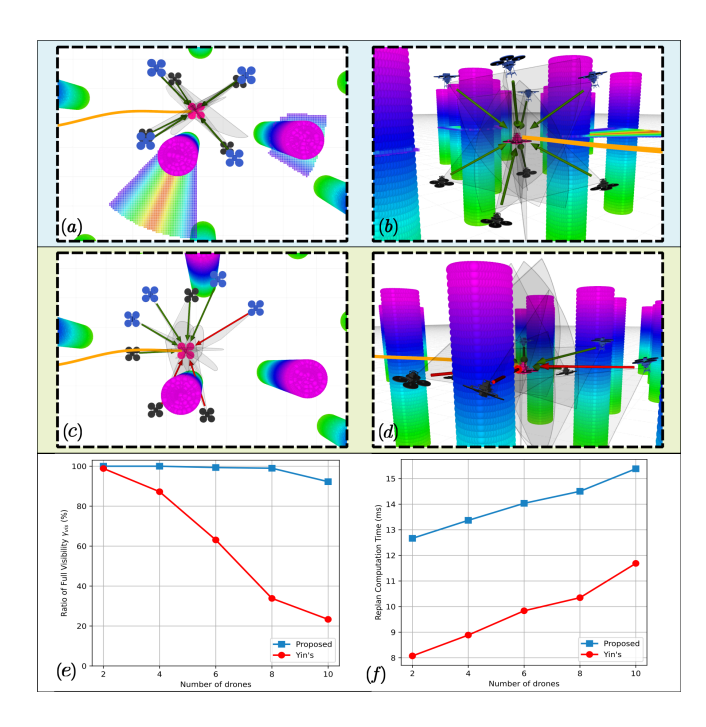


Fig. 14. Results of the swarm size study. (a)-(b) Top-down and side views of the proposed 8-drone tracking behavior, highlighting agile occlusion avoidance with a 3-D polyhedral swarm distribution. (c)-(d) Top-down and side views of the baseline tracking behavior, showing the failure to sustain full swarm visibility. (e) The full-visibility time ratio as the swarm scales up. (f) The computation time per replanning cycle as the swarm scales up.

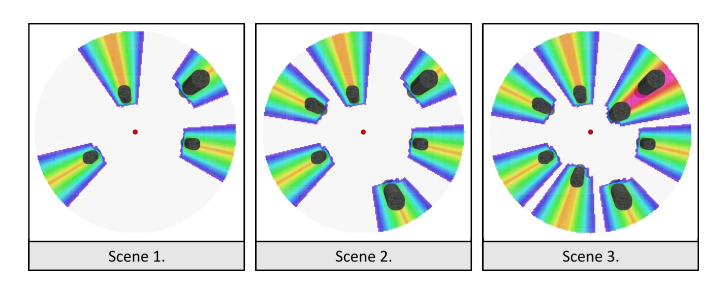


Fig. 15. Top-down views of the test scenes used in the SSDF updating study, along with cross-sections of the updated SSDFs at a height of zero.

replanning time (<16ms) as the swarm size scales up, which is a benefit of their decentralized architectures. The computation time of the proposed method exceeds Yin's by 4-5ms largely due to the SE(3) back-end optimization.

E. Study on SSDF Updating Method

We compare the performance of our incremental SSDF update strategy (Sec.IV-C) against the brute-force traversal approach. The brute-force traversal method iterates along the radial dimension in spherical coordinates $(\theta - \phi - r)$, repetitively applying the 2-D SSDF updating process [11] to each $\theta - \phi$ layer at every radial discretization r. As introduced in Sec.IV-C, our incremental method strategically leverages the monotonic properties of occlusion across adjacent 2-D SSDF layers to reduce the overall update operations.

We construct three scenes with increasing obstacles and set the origin as the target point. The SSDF is parameterized with a 5m radial boundary, 0.1m radial resolution, and 0.1rad angu-

lar resolution. Fig.15 shows the scenes' top-down views and the cross-sections of SSDFs at zero height. The baseline brute-force traversal method [11] provides the ground truth values of updated SSDFs. Tab.II records the average computation time for both approaches and the proposed method's cumulative value error across all grids in the SSDF volume. As shown in Tab.II, the proposed method achieves significantly faster average update time (<4ms) compared to the baseline method (>12ms) with negligible cumulative error. This confirms the efficiency and accuracy of our incremental strategy in enabling real-time SSDF integration for high-frequency replanning.

TABLE II
SSDF UPDATE BENCHMARK RESULTS

Metric Scene	Proposed Update Time (ms)	Baseline Update Time (ms)	Cumulative Value Error (rad)
Scene 1	3.332	12.177	5.32 ×10 ⁻⁶
Scene 2	3.688	12.230	8.31×10^{-6}
Scene 3	4.026	12.391	8.57×10^{-6}

IX. REAL WORLD EXPERIMENTS

A. System Setup and Implementation Details

We integrate the proposed framework with a decentralized LiDAR-based aerial swarm system. The swarm system is composed of autonomous drones with heterogeneous Li-DAR configurations, including upward-facing Mid360 LiDAR, downward-facing Mid360 LiDAR, and Avia LiDAR. Each drone is equipped with a PixHawk flight controller and an onboard computer, the Intel NUC with an i7-12700 CPU. The entire swarm is localized using a decentralized swarm LiDAR-inertial odometry (Swarm-LIO) [26], which provides 100Hz state estimation and 25Hz point clouds for each tracker. All drones are controlled by an on-manifold MPC [29]. The drones communicate with each other via a UDP wireless network. Swarm-LIO handles system clock calibration and global extrinsic transformations for the swarm. Once receiving data from a teammate via UDP, the tracker synchronizes the timestamps and transforms the data from the teammate's frame into its own frame using the global extrinsic. This process is called spatiotemporal alignment.

In the experiments, the targets do not exchange any information with the trackers. It is marked by high-reflectivity materials. The tracker leverages the reflectivity information in LiDAR measurements to detect the target, extracting the largest high-reflection cluster in the point clouds to filter the target out. Once the target position is acquired, the tracker broadcasts its measurement via UDP. The target states are estimated by a constant-velocity Error State Kalman Filter (ESKF). The ESKF fuses the measurements from the ego LiDAR and the spatiotemporally-aligned target measurements from teammates, yielding enhanced target estimation through multi-source fusion. ROG-Map [27] is used for occupancy grid mapping. For a more informed swarm navigation with limited-FOV sensors (e.g., AVIA LiDARs), we extend the environmental perception by employing a bandwidth-efficient map synchronization framework [28], where trackers encode

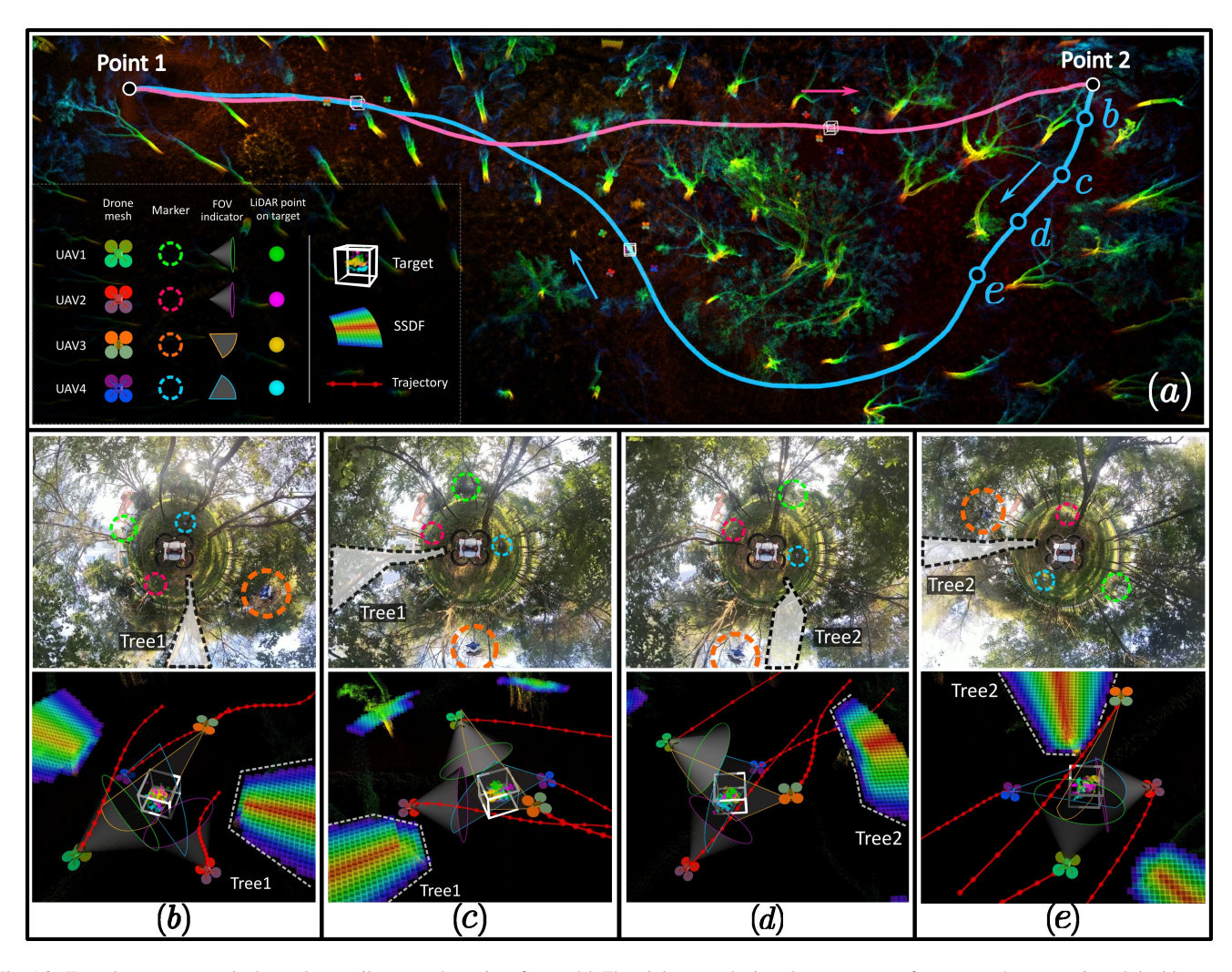


Fig. 16. Four drones cooperatively track an agile target drone in a forest. (a) The pink curve depicts the target route from *Point 1* to *Point 2*, and the blue curve shows the return route. Four keyframes from b to e are selected for further illustration. (b)-(e) Each keyframe includes a snapshot with a 360° camera image (top) and an RViz visualization (bottom). Two tree obstacles, labeled *Tree1* and *Tree2*, along with their corresponding SSDFs, are highlighted to demonstrate occlusion avoidance. The heterogeneous drone FOVs are also visualized to illustrate the FOV compliance.

and compress newly updated map voxels into transmittable chunks [28] and share them via UDP. Receivers then align the shared data spatiotemporally and merge it into their local maps. This approach allows Avia-equipped drones to maintain environmental awareness beyond their native FOV, ensuring safe flight while strictly orienting sensors toward the target. Our planner solves SE(3) trajectory optimization problems using LBFGS-lite [45], executing 15Hz replanning cycles in experiments. Newly planned trajectories undergo immediate broadcasting across the swarm to enable tight coordination. All modules, including estimation, perception, planning, and control, are operating onboard in real-time.

B. Agile Target Tracking in Dense Forest

To validate the real-world performance of our method, we test the tracking system in an unknown dense forest. A heterogeneous LiDAR-based swarm (one upward-facing Mid360, one downward-facing Mid360, and two Avia LiDARs) is deployed. The swarm tracks a manually triggered target drone flying through the forest with a velocity up to 3m/s. The prediction horizon of the target motion is 1.8s.

Fig.16 details the whole swarm tracking task. The target flies from Point 1 to Point 2 in Fig.16(a) and then returns via a distinct route. During the flight, our decentralized swarm performs visibility-aware cooperative target tracking without collisions or occlusions. An Insta360 camera on the target drone records the process. Four snapshots (Figs. 16(b)-(e)) illustrate how the trackers agilely adjust the swarm distribution to avoid LOS blockages by Tree1 and Tree2, leveraging the SSDFs for occlusion-resistant tracking in real scenes. Driven by our joint costs, our decentralized swarm self-organized into a tetrahedron distribution while still ensuring FOV compliance. Tab.III summarizes the average onboard computation time for each stage, including SSDF update (t_{SSDF}), front-end searching (t_{search}) , corridor generation (t_{SFC}) , and back-end optimization (t_{optimize}) . The results characterize the runtime performance of our method in cluttered forest environments. Compared to other LiDAR configurations, drones with Avia LiDARs exhibit longer back-end runtime due to the computational demands of joint yaw trajectory optimization for target alignment.

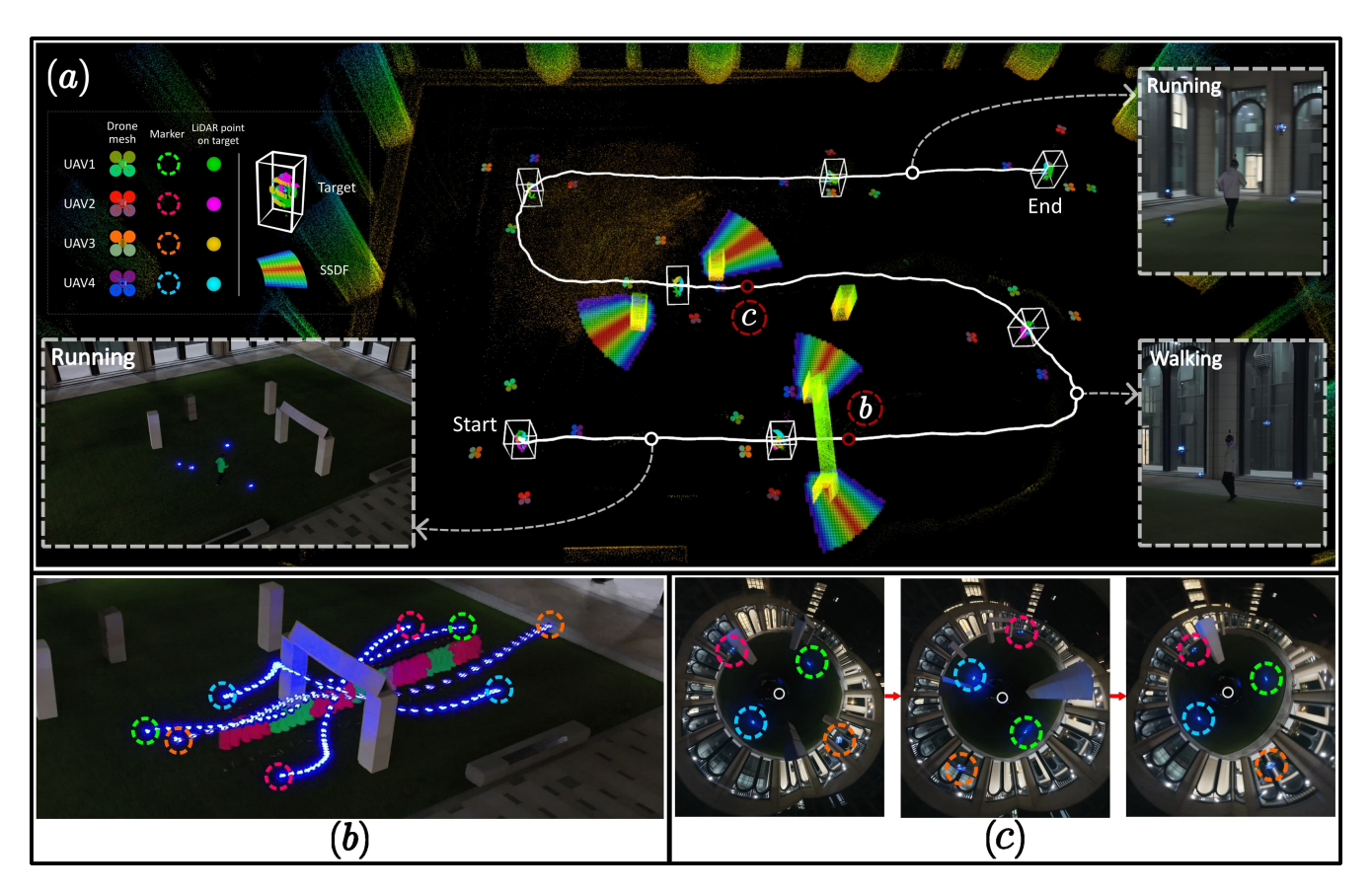


Fig. 17. Four drones cooperatively track a human runner as the target. (a) The write curve depicts the runner's route. Three keyframes along the path are highlighted by the adjacent image snapshots, and two spots, labeled b and c, are marked for detailed illustration in subfigures (b) and (c). (b) A composite image captures the swarm agilely compressing its tracking distribution as the target runs through a gate at spot b. (c) A series of 360° camera snapshots shows the swarm rotating the distribution to prevent occlusion as the target walks through the pillar obstacles at spot c.

TABLE III
AVERAGE ONBOARD COMPUTATION TIME (MILLISECONDS)

	$t_{ m SSDF}$	$t_{ m search}$	$t_{ m SFC}$	$t_{ m optimize}$	$t_{ m total}$
	7.76	0.26	3.17	9.35	20.54
Downward Mid360	7.61	0.22	3.10	8.93	19.86
AVIA	8.53	0.35	3.19	13.20	25.27

C. Cooperative Human Runner Tracking

To further validate our method's practicality, we deploy the swarm system to track a human runner. The runner's motion transitions between walking ($\sim 1m/s$) and running $(\sim 2.5m/s)$. The swarm uses the same LiDAR setup as Sec.IX-B. The runner wears a high-reflectivity vest for fast LiDAR detection. Fig.17(a) shows the scenario and the target route. Fig.17(b) is a composite image recording the swarm motion when the target is running through a gate. To preserve target visibility, the trackers flexibly compress the swarm distribution to traverse the constrained gateway and then elastically resume the tetrahedron tracking formation in open space, demonstrating the agility of our swarm. Fig.17(c) presents Insta360 snapshots when the target walks through pillar obstacles. Driven by SSDFs, the swarm rotates the distribution to avoid occlusions. The swarm's full visibility throughout the target's walking and running phases also confirms the system's reactive adaptation to target velocity changes.

D. Swarm Tracking with Dynamic Joining and Leaving

To demonstrate the system's dynamic swarm reconfigurability, we conduct an experiment that supports teammates joining and leaving during live target tracking. A quadrotor marked by high-reflectivity tapes serves as the target, pursued by four drones (UAV1-4) with heterogeneous LiDAR setups: UAV1 and UAV4 (upward Mid360 LiDARs), UAV2 (downward Mid360 LiDAR), and UAV3 (Avia LiDAR). Fig.18 records the tracking mission. Before starting, UAV1-3 are positioned in area P_1 , where they complete swarm initialization [26] to calibrate extrinsic transformations and form a three-drone swarm. UAV4, placed in area P_2 , begins as an isolated agent, excluded from initial target detection and the swarm.

The mission begins as the target enters area P_1 , where the three-drone swarm detects it and starts cooperative tracking. Although the FOV limitations prevent UAV2 and UAV3 from direct target observation, UAV1 first detects the target and shares its target measurements with UAV2 and UAV3 at once via UDP, facilitating immediate coordinated tracking maneuvers across all agents (Fig.18(b)-(c)). Driven by the swarm distribution cost, the three drones form a triangular encirclement to track the target (Fig.18(d)-(e)). UAV4 remains at its initial position in P_2 and actively attempts to detect the target. When the target enters area P_2 , UAV4 successfully detects it and starts tracking. Since UAV4 has not conducted the prior swarm initialization [26], its extrinsic transformations

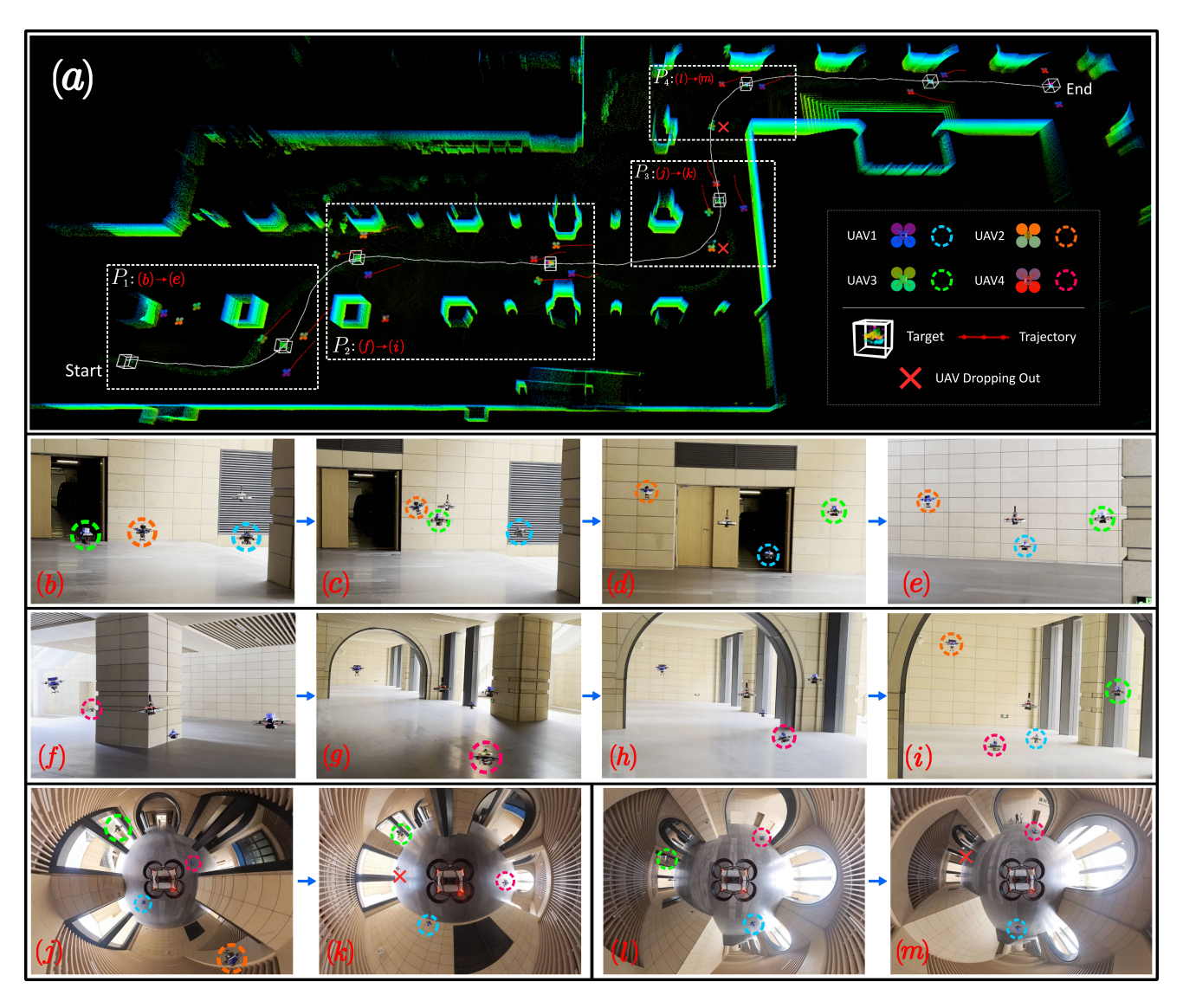


Fig. 18. Swarm tracking experiment with dynamic joining and leaving. (a) The white curve shows the target drone's route. Four areas, labeled as P_1 to P_4 , are marked for further illustration in the following subfigures. (b)-(e): As the target enters area P_1 , the swarm of UAV1-3 detects the target, starts cooperative tracking, and forms a regular triangle distribution. (f)-(i): In P_2 , UAV4 detects the target and initially performs solo tracking in (f)-(g). After the online calibration is complete in (h), UAV4 joins the swarm and then forms a tetrahedron encirclement with its teammates. (j)-(k): In P_3 , the swarm reconfigures the distribution from a tetrahedron to a regular triangle after UAV2 drops out. (j)-(k): In P_4 , the swarm transitions to collinear encirclement after UAV3 leaves.

are not calibrated with the other drones, isolating it from the swarm. Hence, UAV4 tracks the target solo and treats other drones as dynamic obstacles (Fig.18(g)). Meanwhile, the Swarm-LIO modules perform online initialization for UAV4 and the swarm. Once completed, UAV4 joins the swarm (Fig.18(h)) and then forms a new tetrahedron distribution with the other swarm members (Fig.18(i)). As the target enters area P_3 , UAV2 is deliberately terminated to emulate agent failure. The system detects the dropout and adaptively reconfigures the swarm into a regular triangle formation to continue the tracking (Fig.18(j)-(h)). Later, in area P_4 , the swarm size further decreases to two by dropping out UAV3. The left two trackers then form a collinear encirclement to optimize the distribution cost (Fig.18(l)-(m)).

In the experiment, our swarm maintains uninterrupted target tracking during dynamic membership changes, highlighting the system's superior decentralized swarm reconfigurability. The inherent scalability of the proposed swarm tracking cost functions enables automatic adaptation to swarm-size variations without any hardcoded rules. The dropout tests further verify the system's robustness and fault tolerance.

X. CONCLUSION

This paper proposed a systematic solution for visibility-aware cooperative target tracking using decentralized LiDAR-based swarms. To address environmental occlusion, we introduced a Spherical Signed Distance Field (SSDF) that encodes 3-D visibility and supports real-time onboard computation with an efficient update algorithm. Comprehensive differentiable metrics were developed for swarm tracking, notably including FOV-alignment costs for heterogeneous LiDARs and an electrostatic-potential-inspired swarm distribution cost for coordinated 3-D target coverage. These components powered a two-stage planning framework comprising a kinodynamic

searcher and a spatiotemporal SE(3) optimizer, trading off objectives for visibility-aware cooperative swarm tracking. Deployed on real-world LiDAR-based swarms featuring collaborative perception and dynamic reconfigurability, our decentralized system demonstrated robust performance in complex outdoor environments through rigorous experiments.

REFERENCES

- B. F. Jeon and H. J. Kim, "Online trajectory generation of a may for chasing a moving target in 3d dense environments," in 2019 IEEE/RSJ International Conference on Intelligent Robots and Systems (IROS). IEEE, 2019, pp. 1115–1121.
- [2] B. Jeon, Y. Lee, and H. J. Kim, "Integrated motion planner for real-time aerial videography with a drone in a dense environment," in 2020 IEEE International Conference on Robotics and Automation (ICRA). IEEE, 2020, pp. 1243–1249.
- [3] Q. Wang, Y. Gao, J. Ji, C. Xu, and F. Gao, "Visibility-aware trajectory optimization with application to aerial tracking," in 2021 IEEE/RSJ International Conference on Intelligent Robots and Systems (IROS). IEEE, 2021, pp. 5249–5256.
- [4] Y. Gao, J. Ji, Q. Wang, R. Jin, Y. Lin, Z. Shang, Y. Cao, S. Shen, C. Xu, and F. Gao, "Adaptive tracking and perching for quadrotor in dynamic scenarios," *IEEE Transactions on Robotics*, vol. 40, pp. 499–519, 2023.
- [5] J. Ji, N. Pan, C. Xu, and F. Gao, "Elastic tracker: A spatio-temporal trajectory planner for flexible aerial tracking," in 2022 International Conference on Robotics and Automation (ICRA). IEEE, 2022, pp. 47–53.
- [6] X. Zhou, X. Wen, Z. Wang, Y. Gao, H. Li, Q. Wang, T. Yang, H. Lu, Y. Cao, C. Xu et al., "Swarm of micro flying robots in the wild," *Science Robotics*, vol. 7, no. 66, p. eabm5954, 2022.
- [7] L. Yin, F. Zhu, Y. Ren, F. Kong, and F. Zhang, "Decentralized swarm trajectory generation for lidar-based aerial tracking in cluttered environments," in 2023 IEEE/RSJ International Conference on Intelligent Robots and Systems (IROS). IEEE, 2023, pp. 9285–9292.
- [8] Y. Lee, J. Park, and H. J. Kim, "Dmvc-tracker: Distributed multi-agent trajectory planning for target tracking using dynamic buffered voronoi and inter-visibility cells," arXiv preprint arXiv:2411.18086, 2024.
- [9] J. Wang, P. Ren, M. Gong, J. Snyder, and B. Guo, "All-frequency rendering of dynamic, spatially-varying reflectance," in ACM SIGGRAPH Asia 2009 papers, 2009, pp. 1–10.
- [10] R. Wang, M. Pan, W. Chen, Z. Ren, K. Zhou, W. Hua, and H. Bao, "Analytic double product integrals for all-frequency relighting," *IEEE Transactions on Visualization and Computer Graphics*, vol. 19, no. 7, pp. 1133–1142, 2012.
- [11] R. Wang, M. Pan, X. Han, W. Chen, and H. Bao, "Parallel and adaptive visibility sampling for rendering dynamic scenes with spatially varying reflectance," *Computers & graphics*, vol. 38, pp. 374–381, 2014.
- [12] K. Iwasaki, K. Mizutani, Y. Dobasbi, and T. Nisbita, "Interactive cloth rendering of microcylinder appearance model under environment lighting," in *Computer Graphics Forum*, vol. 33, no. 2. Wiley Online Library, 2014, pp. 333–340.
- [13] R. Tallamraju, E. Price, R. Ludwig, K. Karlapalem, H. H. Bülthoff, M. J. Black, and A. Ahmad, "Active perception based formation control for multiple aerial vehicles," *IEEE Robotics and Automation Letters*, vol. 4, no. 4, pp. 4491–4498, 2019.
- [14] X. Liu, K. Liu, T. Hu, and Q. Zhang, "Formation control for moving target enclosing via relative localization," in 2023 62nd IEEE Conference on Decision and Control (CDC). IEEE, 2023, pp. 1400–1405.
- [15] X. Liu, D. Zhang, Q. Zhang, and T. Hu, "Formation control for enclosing and tracking via relative localization," *IEEE Transactions on Aerospace* and Electronic Systems, 2025.
- [16] A. G. Kendall, N. N. Salvapantula, and K. A. Stol, "On-board object tracking control of a quadcopter with monocular vision," in 2014 international conference on unmanned aircraft systems (ICUAS). IEEE, 2014, pp. 404–411.
- [17] H. Cheng, L. Lin, Z. Zheng, Y. Guan, and Z. Liu, "An autonomous vision-based target tracking system for rotorcraft unmanned aerial vehicles," in 2017 IEEE/RSJ international conference on intelligent robots and systems (IROS). IEEE, 2017, pp. 1732–1738.
- [18] Z. Han, R. Zhang, N. Pan, C. Xu, and F. Gao, "Fast-tracker: A robust aerial system for tracking agile target in cluttered environments," in 2021 IEEE International Conference on Robotics and Automation (ICRA). IEEE, 2021, pp. 328–334.

- [19] B. Penin, P. R. Giordano, and F. Chaumette, "Vision-based reactive planning for aggressive target tracking while avoiding collisions and occlusions," *IEEE Robotics and Automation Letters*, vol. 3, no. 4, pp. 3725–3732, 2018.
- [20] R. Bonatti, W. Wang, C. Ho, A. Ahuja, M. Gschwindt, E. Camci, E. Kayacan, S. Choudhury, and S. Scherer, "Autonomous aerial cinematography in unstructured environments with learned artistic decisionmaking," *Journal of Field Robotics*, vol. 37, no. 4, pp. 606–641, 2020.
- [21] T. Michikawa and H. Suzuki, "Spherical distance transforms," in 2008 International Conference on Computational Sciences and Its Applications. IEEE, 2008, pp. 405–412.
- [22] A. Bucker, R. Bonatti, and S. Scherer, "Do you see what i see? coordinating multiple aerial cameras for robot cinematography," in 2021 IEEE International Conference on Robotics and Automation (ICRA). IEEE, 2021, pp. 7972–7979.
- [23] C. Ho, A. Jong, H. Freeman, R. Rao, R. Bonatti, and S. Scherer, "3d human reconstruction in the wild with collaborative aerial cameras," in 2021 IEEE/RSJ International Conference on Intelligent Robots and Systems (IROS). IEEE, 2021, pp. 5263–5269.
- [24] T. Nägeli, L. Meier, A. Domahidi, J. Alonso-Mora, and O. Hilliges, "Real-time planning for automated multi-view drone cinematography," ACM Transactions on Graphics (TOG), vol. 36, no. 4, pp. 1–10, 2017.
- [25] V. Krátkỳ, A. Alcántara, J. Capitán, P. Štěpán, M. Saska, and A. Ollero, "Autonomous aerial filming with distributed lighting by a team of unmanned aerial vehicles," *IEEE Robotics and Automation Letters*, vol. 6, no. 4, pp. 7580–7587, 2021.
- [26] F. Zhu, Y. Ren, L. Yin, F. Kong, Q. Liu, R. Xue, W. Liu, Y. Cai, G. Lu, H. Li et al., "Swarm-lio2: Decentralized, efficient lidar-inertial odometry for uav swarms," *IEEE Transactions on Robotics*, 2024.
- [27] Y. Ren, Y. Cai, F. Zhu, S. Liang, and F. Zhang, "Rog-map: An efficient robocentric occupancy grid map for large-scene and high-resolution lidar-based motion planning," in 2024 IEEE/RSJ International Conference on Intelligent Robots and Systems (IROS). IEEE, 2024, pp. 8119–8125.
- [28] L. Shi, L. Yin, F. Kong, Y. Ren, F. Zhu, B. Tang, and F. Zhang, "Real-time bandwidth-efficient occupancy grid map synchronization for multi-robot systems," in 2024 IEEE/RSJ International Conference on Intelligent Robots and Systems (IROS). IEEE, 2024, pp. 8489–8496.
- [29] G. Lu, W. Xu, and F. Zhang, "On-manifold model predictive control for trajectory tracking on robotic systems," *IEEE Transactions on Industrial Electronics*, vol. 70, no. 9, pp. 9192–9202, 2022.
- [30] P. F. Felzenszwalb and D. P. Huttenlocher, "Distance transforms of sampled functions," *Theory of computing*, vol. 8, no. 1, pp. 415–428, 2012
- [31] A. Meijster, J. B. Roerdink, and W. H. Hesselink, "A general algorithm for computing distance transforms in linear time," *Mathematical Morphology and its applications to image and signal processing*, pp. 331–340, 2000.
- [32] C. R. Maurer, R. Qi, and V. Raghavan, "A linear time algorithm for computing exact euclidean distance transforms of binary images in arbitrary dimensions," *IEEE Transactions on Pattern Analysis and Machine Intelligence*, vol. 25, no. 2, pp. 265–270, 2003.
- [33] D. W. Paglieroni, "A unified distance transform algorithm and architecture," Machine Vision and Applications, vol. 5, no. 1, pp. 47–55, 1992.
- [34] L. Han, F. Gao, B. Zhou, and S. Shen, "Fiesta: Fast incremental euclidean distance fields for online motion planning of aerial robots," in 2019 IEEE/RSJ International Conference on Intelligent Robots and Systems (IROS). IEEE, 2019, pp. 4423–4430.
- [35] D. Zhu, C. Wang, W. Wang, R. Garg, S. Scherer, and M. Q.-H. Meng, "Vdb-edt: An efficient euclidean distance transform algorithm based on vdb data structure," arXiv preprint arXiv:2105.04419, 2021.
- [36] H. Oleynikova, Z. Taylor, M. Fehr, R. Siegwart, and J. Nieto, "Voxblox: Incremental 3d euclidean signed distance fields for on-board mav planning," in 2017 IEEE/RSJ International Conference on Intelligent Robots and Systems (IROS). IEEE, 2017, pp. 1366–1373.
- [37] Y. Pan, Y. Kompis, L. Bartolomei, R. Mascaro, C. Stachniss, and M. Chli, "Voxfield: Non-projective signed distance fields for online planning and 3d reconstruction," in 2022 IEEE/RSJ International Conference on Intelligent Robots and Systems (IROS). IEEE, 2022, pp. 5331–5338.
- [38] M. Watterson and V. Kumar, "Control of quadrotors using the hopf fibration on so (3)," in *Robotics Research: The 18th International* Symposium ISRR. Springer, 2019, pp. 199–215.
- [39] J. Tomson, "On the structure of the atom: an investigation of the stability and periods of osciletion of a number of corpuscles arranged at equal intervals around the circumference of a circle; with application of the results to the theory atomic structure," *Philos. Mag. Series*, vol. 6, no. 7, p. 237, 1904.

- [40] S. Smale, "Mathematical problems for the next century," The Mathematical Intelligencer, vol. 20, pp. 7–15, 1998. [Online]. Available: https://api.semanticscholar.org/CorpusID:1331144
- [41] D. Dolgov, S. Thrun, M. Montemerlo, and J. Diebel, "Practical search techniques in path planning for autonomous driving," ann arbor, vol. 1001, no. 48105, pp. 18–80, 2008.
- [42] S. Liu, N. Atanasov, K. Mohta, and V. Kumar, "Search-based motion planning for quadrotors using linear quadratic minimum time control," in 2017 IEEE/RSJ international conference on intelligent robots and systems (IROS). IEEE, 2017, pp. 2872–2879.
- [43] B. Zhou, F. Gao, L. Wang, C. Liu, and S. Shen, "Robust and efficient quadrotor trajectory generation for fast autonomous flight," *IEEE Robotics and Automation Letters*, vol. 4, no. 4, pp. 3529–3536, 2019.
- [44] S. Liu, M. Watterson, K. Mohta, K. Sun, S. Bhattacharya, C. J. Taylor, and V. Kumar, "Planning dynamically feasible trajectories for quadrotors using safe flight corridors in 3-d complex environments," *IEEE Robotics* and Automation Letters, 2017.
- [45] Z. Wang, X. Zhou, C. Xu, and F. Gao, "Geometrically constrained trajectory optimization for multicopters," *IEEE Transactions on Robotics*, vol. 38, no. 5, pp. 3259–3278, 2022.
- [46] K. L. Teo, V. Rehbock, and L. S. Jennings, "A new computational algorithm for functional inequality constrained optimization problems," *Automatica*, vol. 29, no. 3, pp. 789–792, 1993.